SANDIA REPORT

Microstructural and Continuum Evolution Modeling of Sintering

Veena Tikare, Michael Braginsky, J. Guadalupe Arguello, Terry Garino, Eugene Olevsky, and D. Lynn Johnson

Sandia National Laboratories

Microstructural and Continuum Evolution Modeling of Sintering

Veena Tikare and Michael Braginsky
Materials and Process Modeling and Computation

J. Guadalupe Arguello
Solid Mechanics Engineering

Terry Garino
Ceramic Materials

Sandia National Laboratories
P.O. Box 5800
Albuquerque, NM 87185-1411 USA

Eugene Olevsky
Department of Mechanical Engineering
College of Engineering
San Diego State University
5500 Campanile Drive
San Diego, CA 92182-1323

D. Lynn Johnson
Department of Materials Science & Engineering
Northwest University
2225 N. Campus Dr.
Evanston, IL 60208-3108

Abstract

All ceramics and powder metals, including the ceramics components that Sandia uses in critical weapons components such as PZT voltage bars and current stacks, multi-layer ceramic MET's, alumina/molybdenum & alumina cermets, and ZnO varistors, are manufactured by sintering. Sintering is a critical, possibly the most important, processing step during manufacturing of ceramics. The microstructural evolution, the macroscopic shrinkage, and shape distortions during sintering will control the engineering performance of the resulting ceramic component. Yet, modeling and prediction of sintering behavior is in its infancy, lagging far behind the other manufacturing models, such as powder synthesis and powder compaction models, and behind models that predict engineering properties and reliability. In this project, we developed a model that was

capable of simulating microstructural evolution during sintering, providing constitutive equations for macroscale simulation of shrinkage and distortion during sintering. And we developed macroscale sintering simulation capability in JAS3D.

The mesoscale model can simulate microstructural evolution in a complex powder compact of hundreds or even thousands of particles of arbitrary shape and size by 1. curvature-driven grain growth, 2. pore migration and coalescence by surface diffusion, 3. vacancy formation, grain boundary diffusion and annihilation. This model was validated by comparing predictions of the simulation to analytical predictions for simple geometries. The model was then used to simulate sintering in complex powder compacts. Sintering stress and materials viscous moduli were obtained from the simulations. These constitutive equations were then used by macroscopic simulations for simulating shrinkage and shape changes in FEM simulations.

The continuum theory of sintering embodied in the constitutive description of Skorohod and Olevsky was combined with results from microstructure evolution simulations to model shrinkage and deformation during. The continuum portion is based on a finite element formulation that allows 3D components to be modeled using SNL's nonlinear large-deformation finite element code, JAS3D. This tool provides a capability to model sintering of complex three-dimensional components. The model was verified by comparing to simulations results published in the literature. The model was validated using experimental results from various laboratory experiments performed by Garino. In addition, the mesoscale simulations were used to study anisotropic shrinkage in aligned, elongated powder compacts. Anisotropic shrinkage occurred in all compacts with aligned, elongated particles. However, the direction of higher shrinkage was in some cases along the direction of elongation and in other cases in the perpendicular direction depending on the details of the powder compact. In compacts of simple-packed, mono-sized, elongated particles, shrinkage was higher in the direction of elongation. In compacts of close-packed, mono-sized, elongated particles and of elongated particles with a size and shape distribution, the shrinkage was lower in the direction of elongation.

We also explored the concept of a sintering stress tensor rather than the traditional sintering stress scalar concept for the case of anisotropic shrinkage. A thermodynamic treatment of this is presented. A method to calculate the sintering stress tensor is also presented.

A user-friendly code that can simulate microstructural evolution during sintering in 2D and in 3D was developed. This code can run on most UNIX platforms and has a motif-based GUI. The microstructural evolution is shown as the code is running and many of the microstructural features, such as grain size, pore size, the average grain boundary length (in 2D) and area (in 3D), etc. are measured and recorded as a function of time. The overall density as the function of time is also recorded.

CONTENTS

Chapter 1
Introduction

Veena Tikare, Michael Braginsky and J. Guadalupe Arguello

Sandia manufactures and uses many ceramic components for nuclear weapons, including PZT voltage bars and current stacks, multi-layer ceramic MET's, alumina/molybdenum & alumina cermets, and ZnO varistors. All these ceramics are manufactured by consolidating powders usually by compaction and then sintering the powder compacts. Sandia recently has made exceptional progress in understanding and controlling powder compaction through an integrated materials characterization, computer modeling, and validation program. However, while of equal or greater importance in manufacturing, the ability to predict and control sintering is still in its infancy because the process is so much more complex. We have developed a set of computational tools, which will enable the manufacturing of complex ceramics by predicting structural changes during sintering by incorporating an understanding of the microstructural aspects of sintering into a continuum model.

Sintering is the process by which a compact of individual powder particles weakly held together by inter-atomic forces is fused to form a strong monolithic piece. A powder compact, which typically has 30% to 40% porosity by volume, is sintered by heating it to high temperatures where mass transport between the particles occurs to form a single piece with structural integrity and with other desirable engineering properties. During sintering the porous powder compact will shrink to < 5% porosity and have grains that can be as much as 1 or 2 orders of magnitude larger than the starting particle size. The shrinkage and microstructural changes can lead to significant deformation in the powder compact, often with catastrophic changes that make the component unusable.

A typical, commercially available multi-material, multi-layer ceramic substrate is shown in figure 1. This components is 50 mm x 50 mm x ~10 mm and has between 35 and 50 layers of alumina with metal interconnects that are 3 to 5 μm thick screened on each layer. It also has embedded components such as the capacitor shown in the figure and can also have embedded inductors and resistors. Dimensional tolerances on such ceramics are very tight, demanding excellent control of shrinkage and distortions during sintering. However, the

Figure 1. Schematic diagram of a multi-material, multi-layer ceramic substrate inductors, resistor

ability to predict and control the shape distortions during sintering is poor. Currently, industrial and Sandia manufacturers must spend large amounts of resources to develop the sintering cycle of each component by trial and error. Small changes in the design of each component require a long and costly development cycle.

We have integrate theory, mesoscale modeling and continuum modeling to fundamentally advance our understanding of sintering and our ability to predict macro- and microscopic evolution of the structure in a sintering body. The Potts Monte Carlo model, a statistical-mechanical model, was used to simulate densification, coarsening, diffusion, pore coalescence and migration to simulate microstructural evolution during sintering. We have a developed an novel algorithm to incorporate desification by annihilation of vacancies. This model is a rigorous scientific method that can make the problem of treating thousands of sintering particles tractable on a workstation class computer. Other models currently available for simulating sintering cannot be adapted to solve microstructural evolution on a large scale.

The past and current work in sintering can be divided into two large categories. One set of work treats the microstructural evolution of two or three particles during sintering in great detail[12]. This body of work considers driving forces, transport mechanisms, kinetic factors and geometry to give detailed information about the shapes of the particles and sintering rates during various stages of sintering. Half a century later, current microstructural models of sintering[3] still consider a limited number of particles with idealized shapes. While today's models give more accurate results, they fail, like their predecessors, to treat a macroscopic sintering piece – what is the shape change of, density distribution in, and stress state in a large body?

The second set of work treats the evolution of a macroscopic sintering body. That work considers the sintering part to be a continuum body and applies continuum deformation mechanics to the sintering body to predict shrinkage and shape change. However, the constitutive laws describing sintering of real crystalline materials systems are unknown. Therefore, application of continuum mechanics to sintering real materials systems has been largely unsuccessful[4], despite tremendous improvements in continuum simulation numerical capabilities in recent years.

The model we have developed has the unique capability to bridge the gap between the microstructural models and the continuum models to give an integrated approach to understanding sintering on multiple scales. The kinetic, Monte Carlo model for simulation sintering is a rigorous, science-based model with all the necessary materials physics to predict sintering behavior of a porous body. These mesoscale simulations of sintering provide two important results, (1) constitutive equations used in continuum models to predict shrinkage and shape change of a sintering powder compact and (2) microstructures of sintered compacts for engineering properties evaluation. We have also developed finite element capability to incorporate the constitutive equations generated by the mesoscale model. The integrated capability enables us to predict the shrinkage and shape distortions in a sintering component.

Various aspects of the model are presented in subsequent chapters of this document. Chapter 2 presents the mesoscale model and its validation by comparison to an analytic solution of three particles sintering. Chapter 3 demonstrates how the mesoscale model can be extended to treat multiple particles. Chapter 4 derives the thermodynamic basis for obtaining sintering constitutive relationship from mesoscale simulations for use in continuum simulation. Chapter 5 shows the how the macroscopic simulations of sintering can be done using Sandia's in house code, JAS3D. Finally, Chapter 6 treats the problem of aniostropic shrinkage in powder compacts of elongated particles. These chapters provide an overview of the capabilities we have developed while working on the LDRD project. They also demonstrate how the model can be used to study a host of sintering problem

---

[1]G.C Kuczynski, J. Appl. Phys. 21, 632 (1950); W.D. Kingery and M. Berg, J. Appl. Phys. 26, 1205 (1955); R.L. Coble, J. Am. Ceram. Soc., 41 55 (1958); M.F. Ashby, Acta metall., 22 275 (1974)

[2]

[3]Zeng et al., Mat.Sci.&Eng., A252, 301(1998); Pan et al., Acta metall., 13, 4671 (1998); Zhou & Derby, JACerS, 81, 478 (1998); Bullard, J. Appl. Phys., 81, 159 (1997); Zhang & Scheibel, Acta metall, 43, 4377 (1995) ; Jagota & Dawson, Acta metall., 36, 2551 (1988)

[4] R.K. Bordia and G.W. Scherer, Acta metall. 36, 2393 (1988); E.A. Olevsky, Mat. Sci. & Eng., R23, 41 (1998); A.C.F. Cocks, Acta metall, 42, 2191 (1994); J. Svoboda, H. Riedel and H. Zipse, Acta metall., 42, 435 (1994); H. Riedel, H. Zipse, J. Svoboda, Acta metall., 42 445 (1994).

Chapter 2
Numerical Simulation of Solid State Sintering I: Sintering of Three Particles

Veena Tikare, Michael Braginsky and Eugene A. Olevsky

Abstract

A kinetic, Monte Carlo model, capable of simulating microstructural evolution sintering in a 2D system of three particles, has been presented. The model can simulate several mechanisms simultaneously. It can simulate curvature driven grain growth, pore migration and coarsening by surface diffusion, and densification by diffusion of vacancies to grain boundary and annihilation of these vacancies. Morphological changes and densification kinetics are used to verify the model.

Introduction

Prediction of microstructural evolution during solid state sintering of crystalline materials is difficult. In the simplest case of isotropic energies, single-component, single-phase systems it is still very complex because the details of local geometry are critical in the way they influence thermodynamics and kinetics. Predictions of microstructural evolution were first attempted starting in the 1940's by many. Frenkel treated sintering as a viscous flow phenomena[1]. Kuczynski treated it as a diffusive process[2]. This diffusive approach was adopted by many to refine solid state sintering theories. In general these theories[3,4,5,6,7,8,9] assumed highly idealized geometries of two or three spherical particles or spherical particles on a plate with a number of diffusion paths to analytically predict shrinkage rates. A couple of other simple geometries were also treated[9]. While microstructural evolution and shrinkage rates were predicted by these models, the biggest accomplishment of these models is that they provided insight into the thermodynamics that drives sintering and the influence of transport mechanism that control sintering kinetics. The other big accomplishment of these investigators was the understanding of the role of grain boundaries as the sink for vacancies by annihilation[10,11] due to stresses on grain boundaries exerted by the pores at the grain junctions[7].

The prediction of microstructural evolution during sintering continues to be of great interest. Many numerical simulation techniques have been developed in recent years to study sintering. These include finite element methods[12], a micromechanical approach[13], molecular dynamics simulations[14], continuum thermodynamics solutions[15,16,17] and unit cell solutions[18]. These models continue to provide insights and more accurate solutions to this problem. However, they are still simulations of small, highly simplified systems with limited number of particles. Furthermore, they are not readily extendable to larger, more complex systems consisting of hundreds of particles and therefore limited in their applicability for the study of real systems.

In this paper, we present a kinetic, Monte Carlo model that can simulate sintering in a three-particle system. We make no a priori assumptions about the geometry of the system such as the curvature of the neck or the curvature of the particles; rather the three-

particle system is allowed to evolve under conditions similar to that during sintering. The model is very similar to ones used in the past to simulate many microstructural evolution processes including normal grain growth in single-phase materials[19,20,21], abnormal grain growth, recrystallization[22], phase separation[23], Ostwald ripening [24], pore migration [25,26] and final-stage sintering[27,28]. It has been adapted here to simulate all stages of sintering by adding an algorithm that simulates the formation, diffusion and annihilation of vacancies, which distinguishes it from the previous work of Hassold et al[27]. They modeled final stage sintering by determining the mean distance between pores and eliminating pore sites with a frequency that was in proportion to the mean distance between pores. In this work, vacancies formation, diffusion and annihilation are simulated. We demonstrate the model and its utility by applying it to simulate sintering in a simple geometry. Future work will extend the simulation capability to much larger systems with hundreds of particles.

Model Description

Consider the classical three particle-sintering problem modeled by many previous researchers. In this system, all three particles are circular and of the same size. Sintering in such a system occurs by diffusion of material into the pore, diffusion of vacancies from the pore to the grain boundary and annihilation of the vacancies at the grain boundary. Murch[29] has shown that diffusion can be simulated by random walk in kinetic Monte Carlo models. Furthermore, simulation of long range diffusion in microstructural models similar to the one used here has been shown previously in other works[24,25,26]. We introduce a new algorithm for vacancy annihilation in this work. This vacancy annihilation is applied to the three circular particles sintering geometry to demonstrate that the kinetic Monte Carlo model can simulate sintering.

The model presented here is limited to consideration of the following geometry and processes:
- Three circular particles of equal size sintering as shown in figure 1.
- Grain growth by short range diffusion of atoms from one side of the grain boundary to the other;
- Long range diffusion of material to pores by grain boundary diffusion and along pore surfaces by surface diffusion;
- Vacancy annihilation at grain boundaries.

In the model, an ensemble of grain sites and pore sites is allowed to populate a square lattice. We consider three grains sintering, therefore grain sites can assume one of three distinct, degenerate states, $q_{grain} = [1, 2, 3]$. The pore sites can assume only one state, $q_{pore} = -1$. Contiguous grain sites of the same state q form a grain and contiguous pore sites form a pore. Grain boundaries exist between neighboring grain sites of different states, q, and pore-grain interfaces exist between neighboring pore and grain sites. The equation of state for these simulations is the sum of all the neighbor interaction energies in the system given by

$$E = \frac{1}{2} \sum_{i=1}^{N} \sum_{j=1}^{8} \left(1 - \delta\left(q_i, q_j\right)\right)$$ **Equation 1**

where N is the total number of sites, δ is the Kronecker delta with $\delta(q_i = q_j) = 1$ and $\delta(q_i \neq q_j) = 0$, q_i is the state of the grain or pore at site i and q_j is the state of the nearest neighbor at site j. Thus, the only energy considered in the simulation is the interfacial energy and all unlike neighbors contribute one arbitrary unit of energy to the system. As pore sites can assume only one state, $q_{pore} = -1$, there are no pore boundaries and all pores sites coalesce. In contrast, grain sites can assume many states making grain boundaries possible. This yields a two-component, two-phase system with uniform, isotropic interfacial energies between grains and between grains and pores.

Grain growth is simulated using the method developed in previous works[19,21]. First a grain site is chosen at random from the simulation space. Then a new state q is chosen at random from the three possible states in the system. The grain site is temporarily assigned the new state and the change in energy is evaluated using equation 1. Next the standard Metropolis algorithm[30] is used to perform the grain growth step based on Boltzmann statistics. A random number, R, between 0 and 1 is generated. The transition probability, P, is calculated using

$$P = \begin{cases} \exp\left(\dfrac{-\Delta E}{k_B T}\right) & \text{for} \quad \Delta E > 0 \\ \\ 1 & \text{for} \quad \Delta E \leq 0 \end{cases}$$ **Equation 2**

where k_B is the Boltzmann constant and T is the simulation temperature, a variable that defines the degree of thermal fluctuation in the system. If the $R \leq P$, then the grain growth step is accepted, if not, the original state is restored. The simulation temperature used for grain growth was $k_B T = 0$, which has been shown to simulate grain growth correctly[21].

Pore migration is simulated using conserved dynamics, so that the total number of pore sites and grain sites is the same after a pore migration step. A pore site is chosen and next a neighboring grain site is chosen. The two sites are temporarily exchanged with the grain site assuming a new state q where q results in the minimum energy. This minimum-energy, pore-grain exchange simulates pore migration by surface diffusion[25]. The change in energy for this exchange is calculated using equation 1 and again the standard Metropolis algorithm is used to perform the pore migration step using equation 2 to determine the transition probability. The simulation temperature used for the pore migration step was $k_B T = 0.7$. This higher temperature was necessary to simulate pore migration and is discussed in other works[25,26].

Densification in crystalline solids occurs by uniform annihilation of vacancies at the grain boundaries[31,11]. As vacancies are annihilated, the center of mass of the adjoining grain moves toward the grain boundary, thus giving densification. The rate-

limiting step in this process is for the vacancies to diffuse along the entire length of the grain boundary. In this model a vacancy is defined as a single, isolated pore site that is not connected to any other pore sites. The algorithm used for pore annihilation is the following. A pore site is chosen. If it happens to be a vacancy (an isolated pore site) on a grain boundary, it is annihilated. Annihilation is simulated as follows. A straight line is drawn from the isolated pore site through the center of mass of the adjacent grain to the outside boundary of that particle. Next, the isolated pore site and the outside grain site are exchanged with the grain site assuming the q state of the adjacent grain. This algorithm conserves mass globally, moves the center of mass of the adjacent grain towards the annihilation site, and annihilates a vacancy. The frequency of the annihilation attempts is adjusted to simulate the diffusion of vacancies to the entire grain boundary. As the grain boundary length increases, time between annihilations also increases as:

$$t_{anni} = t_{anni}^{i} \left(\frac{L_{gb}}{L_{gb}^{i}} \right)^2 \qquad \text{Equation 3}$$

where t_{anni} is the time between annihilation attempts, t_{anni}^{i} is the time between annihilation attempts for the initial grain boundary length L_{gb}^{i} at the beginning of sintering, and L_{gb} is the current grain boundary length. Adjusting the annihilation frequency in this manner simulates uniform annihilation of vacancies along the grain boundary.

Time in the model is measured in units of Monte Carlo step; 1MCS corresponds to N attempted changes where N is the total number of sites in the system. MC time is linearly proportional to real time[32] in material systems that have the characteristics simulated by the model. The proportionality constant of a given material can be found by comparing simulated microstructural evolution to that of the material. The starting configuration for the simulation is three circular particles touching each other as shown in figure 1. The grain growth, pore migration and annihilation algorithms are applied as described above to simulate sintering. Three separate simulations were run from the same starting configuration for 150,000 MCS, a time past the disappearance of the center pore. Qualitative microstructural evolution are reported and shrinkage y at time t in the simulation is calculated as:

$$y(t) = \frac{\Delta A}{A_o}(t) = \frac{N_{p,o} - N_p(t)}{N_g + N_{p,o}} \qquad \text{Equation 4}$$

where A_o is the initial area; ΔA is the change in area; $N_{p,o}$ is the initial number of pore sites (the number of pore sites in the middle of the three particles shown in figure 1); $N_p(t)$ is the number of pore sites in the middle of the three particles at time t; and N_g is the total number of grain sites, which remains constant. In addition to microstructural evolution, the shrinkage results of the three simulation runs are averaged and presented in the following section.

Results and Discussion

The microstructural evolution of this three-particle sintering simulation is shown in figure 1. Qualitatively, these results are expected. Initially the three particles are just touching and all three pore edges are completely concave. As sintering progress, the
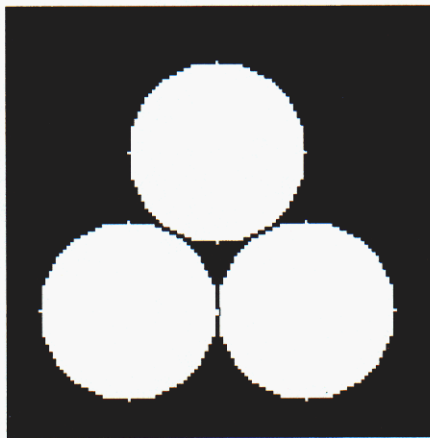
1a
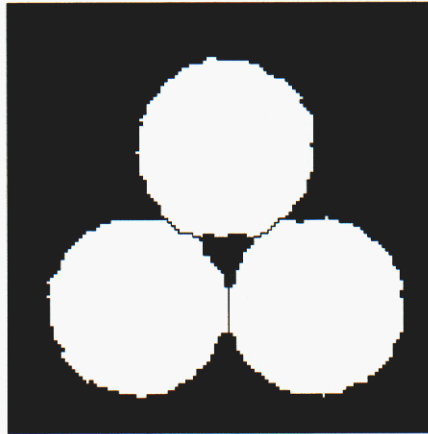
1b
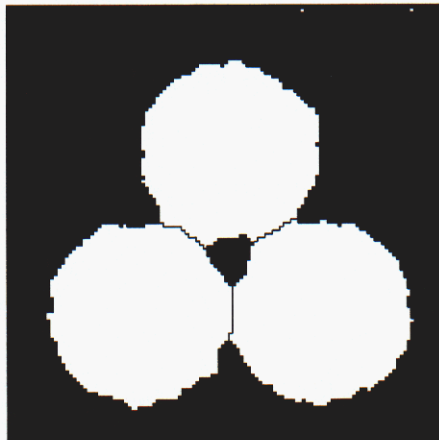
1c
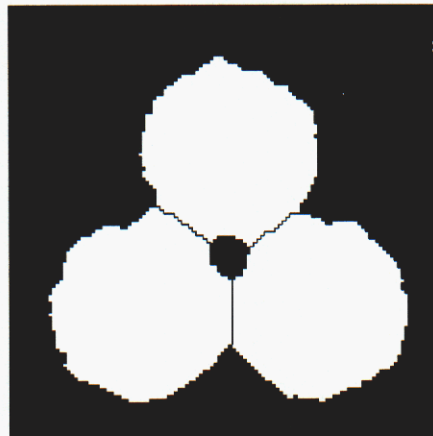
1d
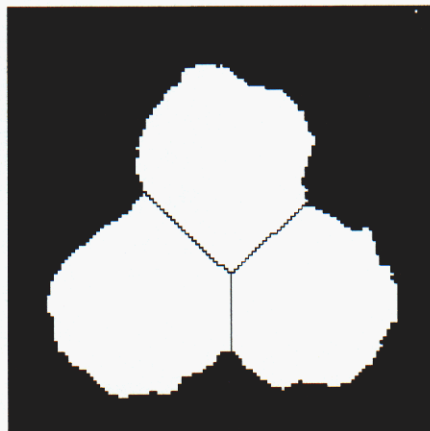
1e

Figure 1. Simulation results showing microstructural evolution during sintering of three particles. The starting microstructure shown in 1a is of three circular particles touching and the last microstructure, 1e, is after the pore disappears.

necks between the grains grow and the pore corners start to round. The pore edges become increasingly convex as the pore shrinks. The centers of mass of the three particles approach each other's. No grain growth is observed and none is expected as the grains are all of the same size and the grain boundaries in between them remain straight as they grow. After the pore in the center disappears, densification continues as the centers of mass of the three particles continue to approach each other.

The morphological characteristics observed were expected, but we wanted to verify that the model could simulate sintering kinetics as well. Kinetics are verified by comparing densification curve of the simulation to that predicted by sintering theory. Shrinkage rate of circular particles sintering has been treated analytically by many[2-7]. They all used a similar approach by equating the flux of the material to neck with the increase in neck size and solved for the shrinkage as a function of sintering time. They reported the time exponent for shrinkage to vary from 0.31 to 0.50 depending on the details of their derivation such as the transport mechanism and curvature they assumed for the pore edge. Here we compare our simulation results with the predictions of Johnson[7] who treated both 3D case (two spheres sintering) and 2D case (two infinitely long wires sintering). He predicted the shrinkage rate by relating the flux of material into the neck to the neck growth for grain boundary diffusion, the same mechanism simulated in this work. The assumptions he made were that particles were infinitely long cylinders of the same size; the radius of curvature of the particles remained constant everywhere (the particles remained cylindrical) except at the neck; the mass transport mechanism is grain boundary diffusion; and the grain boundary between the particles remains straight as it grows. For the 2D case of infinitely long wires, he obtained the following for shrinkage as a function of time

$$y = Br^{-1.32}t^{0.33} \qquad \qquad \textbf{Equation 5}$$

where y is shrinkage, B is a constant related to diffusivity, surface energy, atomic volume, particle radius and other materials parameters, and t is time. The shrinkage in the simulation was calculated using equation 4. The shrinkage was averaged over the three simulation runs. While the simulation was run past the disappearance of the center pore, the shrinkage is calculated from the starting configuration until the center pore disappears. The shrinkage obtained from the simulations is compared to sintering theory in figure 2, a plot of shrinkage as a function of time. As one can see there is very good agreement at early times in the simulation, but at the later time, the simulation shrinks faster than sintering theory would predict. The disagreement in the later time between simulation and theory is due to the assumptions that the pore remained concave as the simulation progressed. Clearly, the pore shape changes from a concave shape to a convex shape as sintering proceeds (see figure 1a to d). This change in shape of the pore was reported by Alexander and Balluffi[11] in their classic paper studying sintering of copper wires.

Figure 2. Shrinkage as a function of time measured in the simulation is compared to the shrinkage predicted by sintering theory, equation (5).
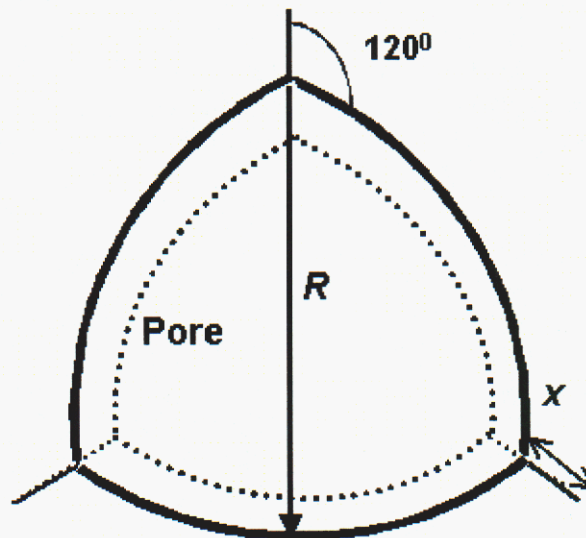
Figure 3. Convex shaped pore used for derivation of densification rate during later times of simulation. The solid line is the shape of the pore at time t_1 and the dotted outline at a later time t_2.

To test the hypothesis that the change in pore shape leads to the discrepancy in shrinkage rate between the simulation and analytical prediction of shrinkage, we analytically calculated the shrinkage as a function of time for the convex pore shape. We made the assumptions similar to the ones made in by the earlier model. The grains

16

remain circular except for the flattening at grain boundaries (have the same radius of curvature everywhere except at the grain boundaries). The pore has the convex shape shown in figure 3 with all three segments having the same curvature. The segments meet at 120° angle since the simulation treats the case of isoenergy surfaces. The pore is assumed to shrink self-similarly with the grain boundaries growing longer as sintering proceeds.

The shrinkage equation was derived for this geometry by equating the flux of material into the pore by grain boundary diffusion to the rate of change in pore area following Johnson's treatment[7]:

$$J\delta = \frac{dA}{dt} \qquad\qquad \textbf{Equation 6}$$

where J is the flux per unit time, δ is the grain boundary thickness, A is the pore area and t is time. The flux is

$$J = -\frac{D\delta}{\Omega kT}\nabla\mu \qquad\qquad \textbf{Equation 7a}$$

where D is the grain boundary diffusivity, Ω is the molar area, k is Boltzmann's constant, and T is temperature. Johnson noted that the quasi-steady state condition requires

$$\nabla J = const \qquad\qquad \textbf{Equation 7b}$$

and that chemical potential and stress are related as

$$\nabla\sigma = \frac{\nabla\mu}{\Omega} \qquad\qquad \textbf{Equation 7c}$$

The solution to the stress (or chemical potential) equation is of the form

$$\sigma = ax^2 + b \qquad\qquad \textbf{Equation 7d}$$

and two boundary conditions are stress at the center of the neck is $\nabla\sigma(x = 0) = 0$, and

stress at the pore surface x_o is $\sigma(x = x_o) = -\frac{2\gamma}{R}$ where γ is the surface energy and R is

pore radius of curvature. Finally, the force balance on the grain boundary requires

$$\int_0^{x_o} \sigma dx = \gamma \sin\left(\frac{\pi}{3}\right) \qquad\qquad \textbf{Equation 7e}$$

Using all the relationships above and noting that the neck size for low porosity is proportional to negative pore radius it can be shown that the flux is

$$J = -\frac{6\gamma\delta D \sin(\pi/3)}{kTR^2} \qquad\qquad \textbf{Equation 8}$$

The pore area is also a function of pore radius

$$A = \frac{R^2}{2}\left(\pi - \sqrt{3}\right) \qquad\qquad \textbf{Equation 9}$$

Substituting Equations 8 and 9 into 6 and solving for R with the boundary condition $R=R_o$ at $t = 0$, where R_o is the initial pore radius, one gets

$$R^4 = R_o^4 - \frac{4\Gamma}{\pi - \sqrt{3}}t \qquad\qquad \textbf{Equation 10}$$

where $\Gamma = -\dfrac{6\gamma\delta^2 D \sin(\pi/3)}{kT}$. The equation describing shrinkage as a function of time is

$$y(t) = \frac{\Delta A}{A_o}(t) = \frac{R_o^2 - \sqrt{R_o^4 - Ct}}{R_o^2} \qquad\qquad \textbf{Equation 11}$$

where $C = \dfrac{4\Gamma}{\pi - 3}$.

Figure 4 compares the shrinkage equation 11 with the results obtained from simulations. There is agreement between the simulation results and the analytically predicted results for this geometry. Furthermore, the microstructures shown in figure 1 are labeled on figure 4 and correspond well with the concave pore shaped region, the transition region and the convex pore-shaped region of figure 4. Therefore, we conclude that the model presented in this work simulates solid-state sintering in crystalline systems with grain boundary diffusion as the transport mechanism well.
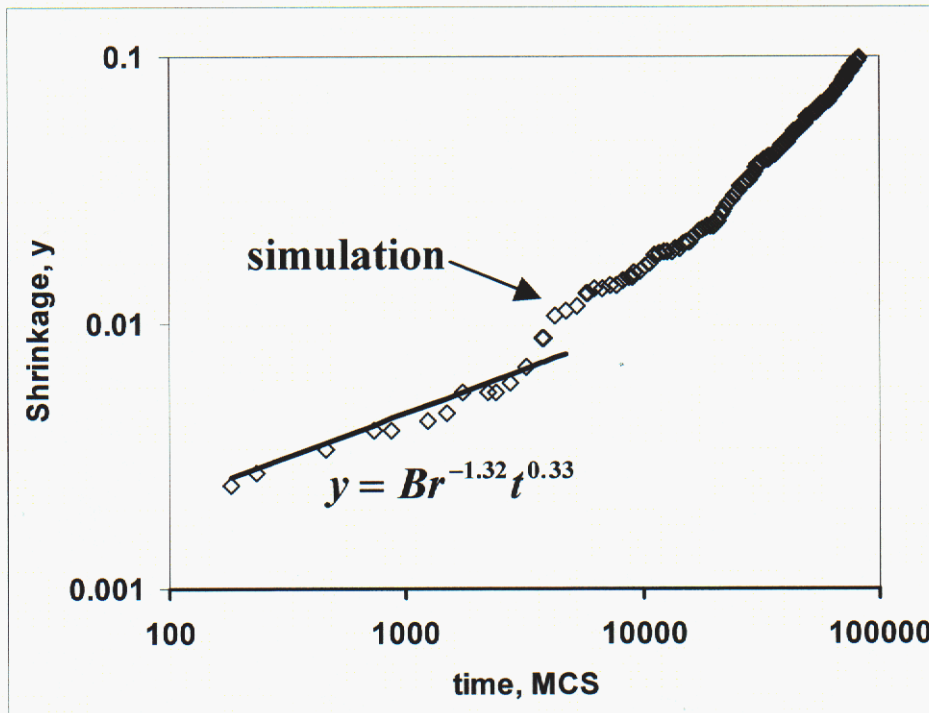

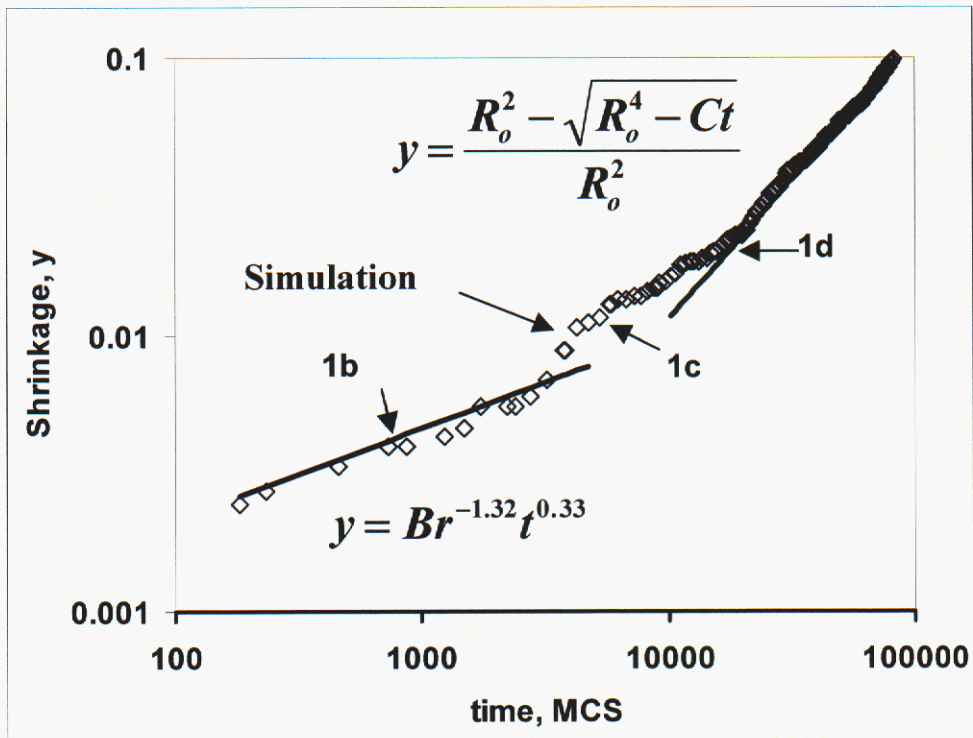Figure 4. Shrinkage as a function of time measured in the simulation is compared to the shrinkage predicted by sintering theory, equation (5) for the concave pore-shaped region and equation (11) for the convex pore-shaped region. The times corresponding to the microstructures shown in figure 1 are labeled.

The model presented here simulates a number of microstructural evolution processes that are driven by the reduction of interfacial free energy. While the model is capable of simulating grain growth, no grain growth occurs in this simulation as the three particles are the same size and there is no curvature to the boundaries between them.

Single pore sites, analogous to vacancies, are formed at all surfaces. As shown elsewhere[33] the concentration of vacancies near an interface is inversely proportional to its curvature as formalized by the Gibbs-Thompson relation. Thus, more vacancies are formed at the internal pore surface than at the outside boundaries of the particles. When these vacancies diffuse to the grain boundary, they are annihilated and densification occurs. Surface diffusion at the pore surface and the external particle surfaces causes the shape of the system to equilibrate constantly, thus leading to minimum energy shapes in the system.

Conclusions

A kinetic, Potts Monte Carlo model, capable of simulating microstructural evolution during sintering in a 2D system of three particles, has been presented. It has been shown to accurately predict the microstructural evolution in such a system by simulating the expected topological changes and by simulating the kinetics of densification. The topological changes are compared to experimental evidence found in the sintering literature. The densification kinetics is compared to predictions of sintering theory.

[1] J. Frenkel, "Viscous Flow of Crystalline Bodies Under the Action of Surface Tension," *J. Phys. (URSS)*, 9 [5] 385-91 (1945).

[2] G.C. Kuczynski, "Self-Diffusion in Sintering of Metallic Particles," *Trans. AIME*, 185, 169-178 (1949)

[3] W.D. Kingery and M. Berg, "Study of the Initial Stages of Sintering Solids by Viscous Flow, Evaporation-Condensation and Self-Diffusion, "*J. Appl. Phys.* 26 1205-1212 (1955)

[4] D.L. Johnson and I.B. Cutler, "Diffusion Sintering: I, Initial State Sintering Models and Their Application to Shrinkage of Powder Compacts," *J. Amer. Ceram. Soc.* 46 541(1963).

[5] D.L. Johnson and T.M. Clarke, "Grain Boundary and Volume Diffusion in the Sintering of Silver," *Acta Metal.*, 12 1173-1179 (1964).

[6] R.L. Coble, "Initial Sintering of Alumina and Hematite," *J. Amer. Ceram. Soc.* 41 55 (1958)

[7] D.L. Johnson, "New Method of Obtaining Volume, Grain-Boundary, and Surface Diffusion Coefficients from Sintering Data," *J. Appl. Phys.*, 40 [1] 192-200 (1969).

[8] H.E. Exner, "Principles of Single Phase Sintering," *Rev. Powder Metall. Phys. Ceram.*, 1 7 (1979).

[9] F.A. Nichols and W.W. Mullins, "Morphology Changes of a Surface of Revolution due to Capillarity-Induced Surface Diffusion", *J. Applied Phys.* 36 1826 (1965).

[10] J.E. Burke, "Role of Grain Boundaries in Sintering," *J. Am. Ceram. Soc.*, 40 [3] 80-85 (1957).

[11] B.H. Alexander and R.W. Balluffi, "The Mechanism of Sintering of Copper", *Acta Metall.* 5, 666-677 (1957).

[12] H. Zhou and J.J. Derby, "Three-Dimensional Finite-Element Analysis of Viscous Sintering," *J. Am. Ceram. Soc,* 81 [3] 533-540 (1998).

[13] A. Jagota and P.R. Dawson, "Micromechanical Modeling of Powder Compacts-I. Unit Problems for Sintering and Traction Induce Deformation," *Acta Metall.*, 36 [9] 2551-2561 (1988).

[14] P. Zeng, S. Zajac, P.C. Clapp and J.A. Rifkin, "Nanoparticle Sintering Simulations," *Mat.Sci.&Eng.,* A252, 301–306 (1998).

[15] H.E. Exner, "Neck Shape and Limiting GBD/SD Ratios in Solid State Sintering," *Acta Metall.* 35 587-591 (1987).

[16] J. Pan, H. Le, S. Kucherenko and J.A. Yeomans, "A Model for the Sintering of Spherical Particles of Different Sizes by Solid State Diffusion," *Acta Mater.*, 46 [11] 4671-4691 (1998).

[17] W. Zhang and J.H. Scheibel, "The Sintering of Two Particles by Surface and Grain Boundary Diffusion – A Two-Dimensional Numerical Study," *Acta metall*, 43, 4377-4386 (1995).

[18] J. Svoboda and H. Riedel, "New Solution Describing the Formation of Interparticle Necks in Solid-State Sintering," *Acta Metall. Mater.*, 43 (1995)

[19] M.P. Anderson, D.J. Srolovitz, G.S. Grest, and P.S. Sahni,, "Computer Simulation of Grain Growth - I. Kinetics," *Acta Metall.* 32 [5] 783-791 (1984).

[20] J. Wejchert, D. Weaire, J.P. Kermode, "Monte Carlo Simulation of the Evolution of a Two-Dimensional Soap Froth," *Phil. Mag. B*53 15-24 (1986).

[21] E.A. Holm, James A. Glazier, D.J. Srolovitz, G.S. Grest, "Effects of Lattice Anisotropy and Temperature on Domain Growth in the Two-Dimensional Potts Model," *Phys. Rev. A*, 43 [6] 2662-2668 (1991).

[22] D.J. Srolovitz, G.S. Grest, M.P. Anderson, and A.D. Rollett, *Acta Metall.*, 36 [8] 2115-2128 (1988).

[23] T.T. Rautianinen and A.P. Sutton, "Influence of the atomic diffusion mechanism on morphologies, kinetics, and the mechanisms of coarsening during phase separation," *Phys. Rev. B.* 59 [21] 13681 – 92 (1999).

[24] V. Tikare and J.D. Cawley, "Numerical Simulation of Grain Growth in Liquid Phase Sintered Materials II. Study of Isotropic Grain Growth," *Acta Metall.*, 46[4] 1343-1356 (1998).

[25] V. Tikare and E.A. Holm, "Simulation of Grain Growth and Pore Migration in a Thermal Gradient," *J. Am. Ceram. Soc.*, 81[3] 480-484 (1998).

[26] V. Tikare, M.A. Miodownik, E.A. Holm, "Three-Dimensional Simulation of Grain Growth in the Presence of Mobile Pores," *J.Am. Ceram. Soc.*, 84 [6] 1379-1385 (2001).

[27] G.N. Hassold, I-W, Chen. D.J. Srolovitz, "Computer Simulation of Final-Stage Sintering : I, Model, Kinetics, and Microstructure" *J. Am. Ceram. Soc.*, 73 [10]2857-64 (1990).

[28] I-W. Chen, G.N. Hassold and D.J. Srolovitz, "Computer simulation of final-stage sintering: II, Influence of initial pore size," *J. Am. Ceram. Soc.*, 73 [10] 2865 (1990).

[29] G.E. Murch, "Simulation of Diffusion Kinetics with the Monte Carlo Method," pp 379-427, *Diffusion in Crystalline Solids* ed. by G.E. Murch and A.S. Nowick, Academic Press, (1984).

[30] N. Metropolis, A.W. Rosenbluth, M.N. Rosenbluth, A.N. Teller and E. Teller, "Equation of State Calculations by Fast Computing Machines," *J. Chem. Phys.*, 21 1087-1092 (1953).

[31] R.T. DeHoff, "Stereological Theory of Sintering," *Science of Sintering* ed. by D.P. Uskokovic et al, 55-71, Plenum Press, New York (1989)

[32] Y. Limoge and J.L. Bocquet, "Monte Carlo Simulation in Diffusion Studies: Time Scale Problem," *Acta Metall.* 36 [7] 1717-1722 (1988).

[33] V. Tikare and J.D. Cawley, "Application of the Potts Model to Simulation of Ostwald Ripening," *J. Am. Ceram. Soc.*, 81 [3] 485-91 (1998).

Chapter 3

Numerical Simulation of Solid State Sintering II: Sintering of a Powder Compact

Michael Braginsky and Veena Tikare

Abstract

This chapter discusses in detail the development of a numerical model capable of simulating microstructural evolution during sintering of complex powder compacts. The model based on the kinetic Monte-Carlo (Potts) approach simulates grain growth, vacancy diffusion, and pore annihilation at grain boundaries. Several algorithms for modeling of vacancy annihilation are tested and the most promising is chosen for further development. Results of simulations for perfect close-packed and random starting configurations are presented and discussed.

Introduction

The main purpose of this work is to develop a model capable of simulating microstructural evolution during sintering of a geometrically complex powder compact comprising hundreds of arbitrary-shaped particles. The need for such a model can hardly be overstated. Although great progress has been made in the last 50 years in understanding microstructural evolution during sintering, current models of sintering [1-7] still consider highly idealized geometries with limited number of circular or spherical particles. While these models have provided much insight into the sintering process by predicting shrinkage rates, geometric changes in the particles and other information, their ability to predict characteristics of a complex powder compact has remained limited. We will present a model that is capable of simulating coarsening and densification in a powder compact at all stages of sintering. This capability will allow us to predict density distribution and shape changes in a large body.

There is a great number of works treating complex diffusion and transport mechanisms during different stages of sintering [8-12], usually applied to a rather limited number of particles or particular geometries. For instance, Ashby [25] assumes sintering of a powder compact consisting of spherical particles of single size and uses statistical methods of [25-28] to determine the number of contact neighbors, sintering pressure, and densification. More recent analytical and numerical models of sintering make fewer assumptions and are able to treat the details of shape change, shrinkage rate or other characteristic more accurately in a sintering compact. These works lead to greater understanding of the sintering process and to better predictive models of sintering. However, they do not capture the complexity of a real sintering system. Furthermore, these models treat each stage of sintering based on a different set of assumptions, while it would be beneficial to have a unified model capable of treating all the stages of sintering based on the underlying physics.

The model used to simulate sintering in this work is based on the kinetic Monte-Carlo (Potts) model [15], which was used successfully to model grain growth and pore migration previously [16-18]. Hassold et al. [20] used a similar kinetic Monte Carlo model to simulate final stage sintering, by

resizing the pores based on the mean distance between pores. Rather than shrink pores, as Hassold et al. [20] did, we simulate the formation, diffusion, and annihilation of vacancies. A vacancy annihilation mechanism based on the view developed in the stereological theory of sintering [19] is added to the model in order to simulate densification. This mechanism comprises vacancy migration from the pores to grain boundaries and vacancy annihilation at the boundaries. The annihilation occurs at a uniform rate along the grain boundary and yields densification. Centers of mass of adjacent grains move closer together in the process. The methodology was applied to sintering of three particles in chapter 1. In this chapter we extend the model to simulate sintering in a complex powder compact consisting of a large number of particles of arbitrary shape. All simulation results presented are obtained in 2D.

Potts Model

A kinetic Monte Carlo model [15] was used to simulate 2D microstructural evolution during sintering. It can model the following processes:

1. Grain growth by short range diffusion of atoms from one side of the grain boundary to the other;
2. Long range diffusion of pores by surface diffusion and of vacancies/material by grain boundary diffusion;
3. Vacancy annihilation at grain boundaries[i].

In the model, an ensemble of grain sites and pore sites is allowed to populate a square lattice. The grain sites can assume one of Q distinct, degenerate states, where the individual state is designated by the symbol q and the total number of states in the system is Q, $q_{grain} = [1,2,...Q]$. The pore sites can assume only one state, $q_{pore} = -1$.

Contiguous grain sites of the same state q form a grain and contiguous pore sites form a pore. Grain boundaries exist between neighboring grain sites of different states, q, and pore-grain interfaces exist between neighboring pore and grain sites. The equation of state for these simulations is the sum of all the neighbor interaction energies in the system given by

$$E = \frac{1}{2}\sum_{i=1}^{N}\sum_{j=1}^{8}\left(1 - \delta(q_i, q_j)\right)$$

Eq. (1)

where N is the total number of sites, $\delta(q_i, q_j)$ is the Kronecker delta with $\delta(q_i = q_j) = 1$ and $\delta(q_i \neq q_j) = 0$, q_i is the state of the grain or pore at site i and q_j is the state of the nearest neighbor at site j. Thus, the only energy considered in the simulation is the interfacial energy and all unlike neighbors contribute one arbitrary unit of energy to the system. As pore sites can assume only one state, $q_{pore} = -1$, there are no pore boundaries and all pores sites coalesce. In contrast, grain sites can assume many different states making grain boundaries possible. This

---

[i] **In this approximation we refer to a single pore site as a vacancy, while denoting more than one contiguous pore sites as a pore**

yields a two-component, two-phase system with uniform, isotropic interfacial energies between grains and between grains and pores.

Grain growth is simulated using the method developed in previous works[16-18]. First a grain site is chosen at random from the simulation space. Then a new state q is chosen at random from the Q possible states in the system. The grain site is temporarily assigned the new state and the change in energy is evaluated using (1). Next the standard Metropolis algorithm is used to perform the grain growth step based on Boltzmann statistics. A random number, R, between 0 and 1 is generated. The transition probability, P, is calculated using

$$
P = \begin{cases} \exp\left(\dfrac{-\Delta E}{k_B T}\right) & for \quad \Delta E > 0 \\ \\ 1 & for \quad \Delta E \leq 0 \end{cases}
$$

Eq. (2)

where k_B is the Boltzmann constant and T is temperature. If the $R \leq P$, then the grain growth step is accepted, if not, the original state is restored. The simulation temperature used for grain growth was $k_B T = 0$, which has been shown to simulate grain growth well[16-18].

Pore migration is simulated using conserved dynamics, so that the total number of pore sites and grain sites is the same after a pore migration step. A pore site is chosen and next a neighboring grain site is chosen. The two sites are temporarily exchanged with the grain site assuming a new state q where q results in the minimum energy. This minimum-energy, pore-grain exchange simulates pore migration by surface diffusion[21]. The change in energy for this exchange is calculated using (1) and again the standard Metropolis algorithm is used to perform the pore migration step using (2) to determine the transition probability. The simulation temperature used for the pore migration step was $k_B T = 0.7$. This higher temperature was necessary to simulate pore migration and is discussed in another work[21]. Time in the Potts model is measured in units of Monte Carlo steps (MCS); 1MCS corresponds to N attempted changes where N is the total number of sites in the system.

Vacancy, for the purposes of this work, is defined as a single pore site surrounded by grain sites. Vacancy annihilation was simulated in the previous work, sintering of three particles, by exchanging the vacancy with a grain site. The grain site for this annihilation event was selected by drawing a straight line from the isolated pore site through the center of mass of the adjacent grain to the outside boundary of that particle. This algorithm conserves mass globally, moves the center of mass of the adjacent grain towards the annihilation site, and annihilates a vacancy. Extending this algorithm to a large system with many particles is not trivial as very few grains have an external surface. The development of the annihilation algorithm will be presented in the following section.

Model development for microstructural evolution with densification.

Our model incorporates the concept of densification developed in the stereological theory of sintering [19]. In this approach, the densification mechanism comprises vacancy migration from pores to grain boundaries and vacancy annihilation at the grain boundaries. DeHoff [19] visualized this process as vacancies being painted on the grain boundary, with an entire monolayer of vacancies annihilated, so that the centers of mass of adjacent grains move towards that grain boundary. The rate of the process is limited by the time needed for vacancies to diffuse and cover the entire grain boundary. This process is simulated as follows. A pore site is chosen and, if it happens to be an isolated pore site — a vacancy[ii] — in contact with a grain boundary, it is annihilated. We examined several different algorithms for simulating annihilation. All the algorithms were required to conserve mass globally and to move the centers of mass of the grains adjacent to the site being annihilated closer together. The frequency of annihilation attempts is adjusted inversely proportionally to the average length of grain boundaries, as given by:

$$t \propto \left(\frac{L_{gb}}{L_0} \right)^2$$

Eq. (3)

to simulate uniform annihilation along grain boundaries.

First, the three algorithms investigated for vacancy annihilation are described. Next, the densification curves and other microstructural details resulting from these three algorithms are compared. .

- ## The jump algorithm

In this algorithm, pore annihilation is simulated by exchanging a vacancy (an isolated

---

ii In the following we refer to contiguous collections of pore sites as pores, while the term "vacancy" is used to denote single pore sites.
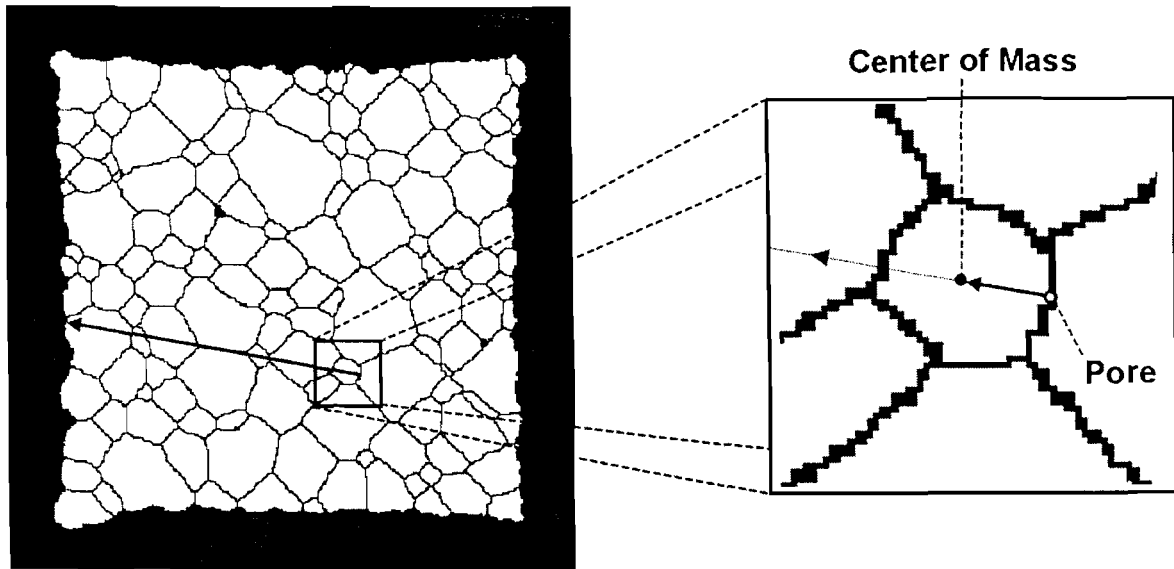
Figure 1. Schematic of the jump algorithm.
Black color denotes pores and grain boundaries; white denotes grains

pore site) at a grain boundary with a grain site at the surface. The grain site for the exchange is chosen at the intersection of a line, drawn from the isolated pore site through the center of mass of the adjacent grain, and the outside boundary of the sintering compact. After the exchange the grain site assumes the q state of the adjacent grain. With "jumps" to the outer boundaries of the compact being simulated this routine to a great extent homogenizes local deformation. The schematic of this algorithm is shown in figure 1.

For this algorithm to work there has to be a surface. Thus, periodic boundary conditions cannot be used.

• The shift algorithm

Like the jump algorithm we start by drawing a line from the isolated pore site through the center of mass of the adjacent grain to the outside boundary of the sintering compact. But in this approach the adjacent grain site on this line fills the isolated pore site. The next site on the line, in turn, replaces the moved grain site, and so on. All the sites on the line (grain and pore sites equally) are shifted towards the site of the annihilated pore. The annihilation step, thus, requires more computational steps to accomplish than in the simpler jump approach

• The shift-with-minimization algorithm

This algorithm is identical to the shift algorithm with one important addition. Each shifted grain site assumes the q state that minimizes the number of unlike neighbors, while pore sites remain pores after shifting. The energy of the system, given by the neighbor interaction energies, is reduced by the minimization of the number unlike neighbors and, therefore, is

smaller after a shift-with-minimization event than after a shift event. This algorithm introduces less distortion into the system.

Comparison of the three algorithms

First we performed simulations with perfect close-packed circular particles as the starting configuration. Microstructures and densification curves showing the dependence of the density of a compact on time were very similar for all three algorithms. Because microstructures resulting from all three algorithms are so similar, only the microstructures produced by the jump algorithm at different times are shown in figure 2. Time, as is customary in such simulations, is measured in Monte-Carlo steps.

Microstructures shown in figure 2 are qualitatively quite similar to the classic experimental results of Alexander and Baluffi [30] on sintering of copper wires. As time progresses pores become smaller due to the vacancies diffusion along grain boundaries and their subsequent annihilation, centers of mass of adjacent grains come closer together. Internal grains stay the same size since grain boundaries between them have no curvature. They attain the hexagonal equilibrium shape as is expected. External grains, which cannot become hexagonal, tend to decrease in size to reduce the free surface area and, hence, the energy of the system.

The densification curves are shown in figure 3. Like the microstructures, all three curves are very similar. The shift algorithm results in a slightly higher densification rate, while the shift-with-minimization leads to a slower densification. The jump algorithm results in the lowest densification rate. The difference in the densities between the three algorithms at all times is less than one percent of initial density.

One potential artifact of the model is a possibility of artificial size differences between exterior and interior grains. In order to check whether this occurs, we calculate average sizes of exterior and interior grains. These separate statistics shown in figure 4 are needed to understand whether replacing pores with grain sites from the boundary alters the grain size statistics in any significant way. In the simulations the largest differences between these sizes were found for the jump algorithm. These differences are rather small (less than 5%) relative to the average grain size during the simulation. In addition, due to the tendency of outer grains to decrease in size to minimize the energy of the system discussed above, only a part of this difference may be attributed to the possible artifact of the model.
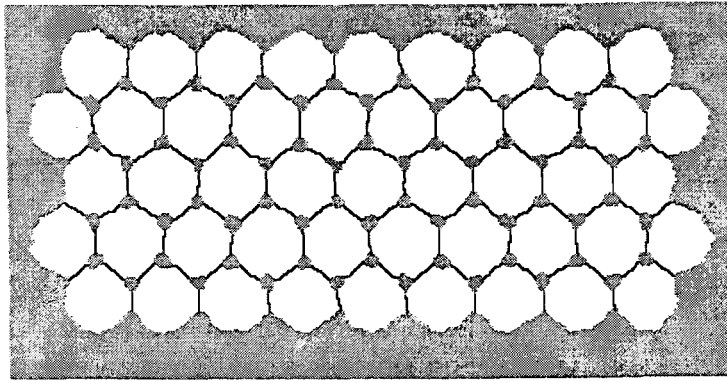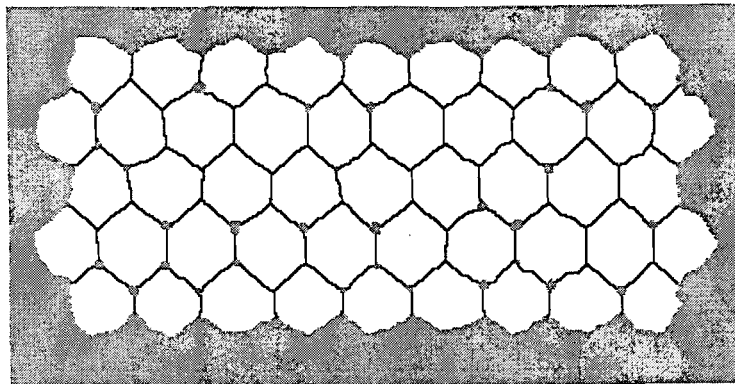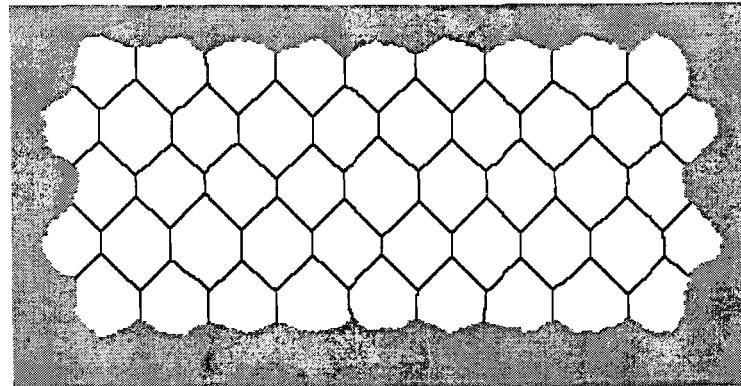
Figure 2. Microstructures obtained using the jump algorithm from a perfect close-packed starting configuration: (a) after 10^4 MCS, (b) after 3×10^4 MCS, and (c) after 10^5 MCS

Thus, all three proposed algorithms perform well for a perfect close-packed initial configuration and lead to reasonable results.
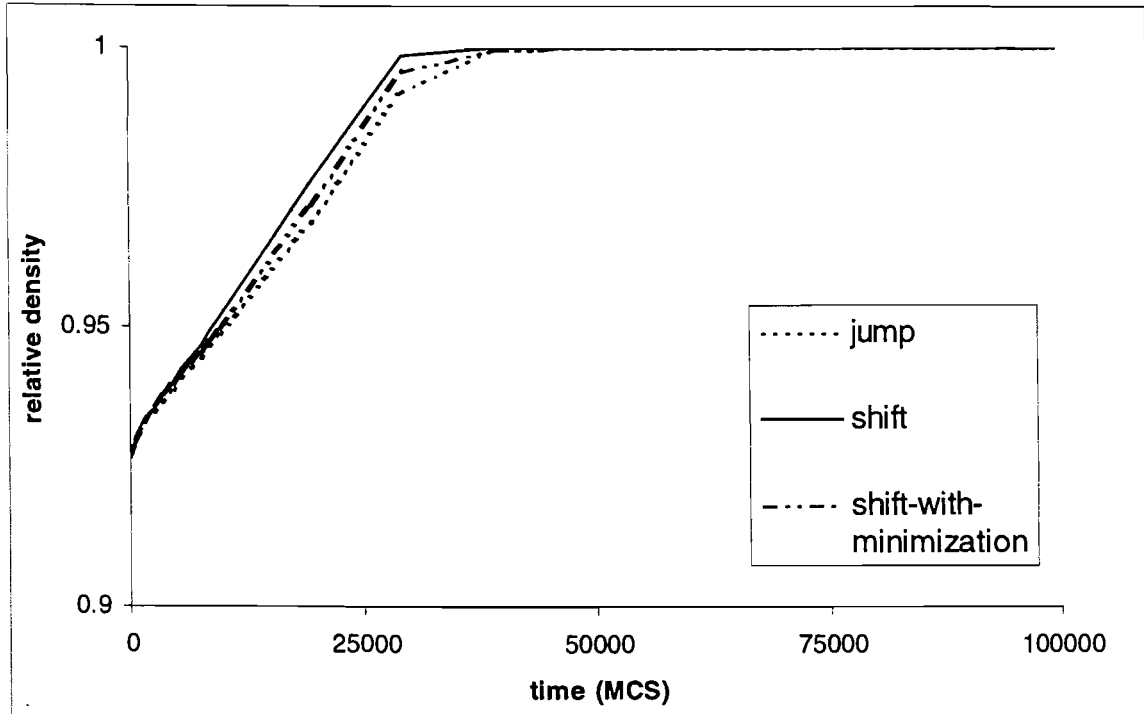
Figure 3. Densification curves for different routines starting from the packed initial configuration

In order to test the methodology further, we performed calculations with randomly packed equi-axed particles of different sizes and with higher initial porosities. As was expected, these simulations revealed much larger discrepancies between the results of the three algorithms, both in terms of densification rates and microstructures, than in the case of the perfect close-packed initial configuration.

As in the previous simulations vacancies diffuse along the grain boundaries and pores shrink due to annihilations, but, unlike the case of a close-packed initial configuration of same size particles that resulted in straight grain boundaries, systems with a random starting configuration exhibit pore and grain coarsening driven by the curvature of grain boundaries. These developments are present in the simulations with all three algorithms, but are somewhat more pronounced, especially the coarsening of pores, in the jump algorithm because, as discussed below, both shift algorithms lead to faster densification. In all three cases grain growth accelerates as pores are being annihilated, which suggests, as expected, that grain coarsening is pinned by pores.

The densification curves and microstructures at different times are shown in figures 5 and 6, respectively. Unlike the previous case of close-packed uniform particles, the densification rate and microstructural evolution resulting from the three algorithms are very different. The microstructures for the shift algorithm are shown for 500, 800, and 1000 Monte-Carlo steps (MCS), with the evidence of densification clear already after 800 MCS and full densification above 2000 MCS, while the first microstructure shown for the jump algorithm at 10000 MCS shows very little densification. Thus, densification in the shift algorithm is orders of magnitude

faster than densification in the jump algorithm, with shift-with-minimization algorithm falling in between.
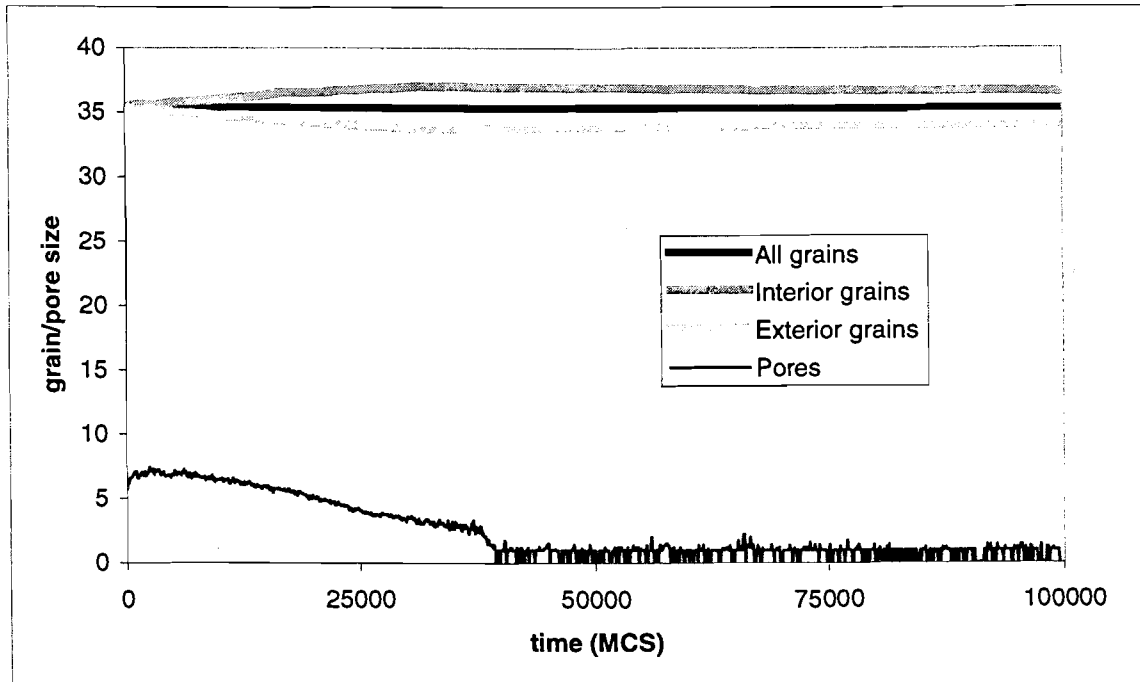
Figure 4. Grain and pore-size statistics for densification from the perfect close-packed starting configuration in the jump algorithm. Average sizes are shown as function of time (in MCS).

Another noticeable difference in microstructures shown in figure 6 is that pores in the microstructures produced by the shift algorithm are rather small during the whole simulation; they are annihilated faster than they coarsen. Full densification in both shift and shift-with-minimization algorithms is achieved at significantly smaller grain sizes than in the jump algorithm.

The reason for much higher densification rates in the shift algorithm is that, as evidenced by the microstructures shown, shifting artificially introduces lots of vacancies into the system at or close to grain boundaries. In addition, the energy of the system is increased significantly because shifted grain and pore sites are more likely to have a higher number of unlike neighbors after the shift. It is analogous to introducing artificial noise into the system by producing too many vacancies. Thus, annihilation events are much more probable, which leads to rapid densification. The situation is analogous to noise-induced transition [23], when the behavior of a physical system far from equilibrium is dramatically changed because of noise. The main difference, though, is that in the shift algorithm "noise" is introduced into the model system artificially, in the computation only, with no apparent analog in the physical realm. The shift-with-minimization algorithm introduces less artificial noise as seen in the microstructures in figure 6 and densification curves in figure 5. Additional energy minimization during shifting makes the resulting microstructures less erratic, with the artificial energy increase due to shifting

significantly smaller than produced by the shift algorithm. However, pores along the line of shift are moved and some become vacancies in the shift-with-minimization algorithm as well leading . to higher densification rates than in the jump algorithm.

Unlike both shift algorithms, annihilation in the jump algorithm almost always decreases the energy of the system. The number of unlike neighbors after a substitution of a grain site for a vacancy in this algorithm can increase at most by 2 or decrease by as many as 14 depending on the configuration with both extreme values unlikely. This results in much more reasonable microstructures than in both shift algorithms.

Thus, based on the analysis of the microstructures and densification curves, we can state unequivocally that the jump algorithm leads to more reasonable results, while both shift algorithms produce physically unrealistic microstructures due to "noise" artificially introduced by the algorithms. In addition, both shift algorithms, especially, the shift-with-minimization, require more computational time. Therefore, the jump algorithm is chosen for the subsequent development.

As stated above, one of our concerns was the possibility that the proposed algorithms alter grain size statistics. figure 7 shows grain and pore size statistics for the simulation from a random initial configuration with the jump algorithm. Here, unlike the case of perfect packing, the difference in grain size of exterior and interior grains is more pronounced, especially, if we consider relative sizes. Nevertheless, grain growth of all grains including exterior grains, as evidenced by figure 7, is much higher than the rate of exterior grain shrinkage due to annihilation.
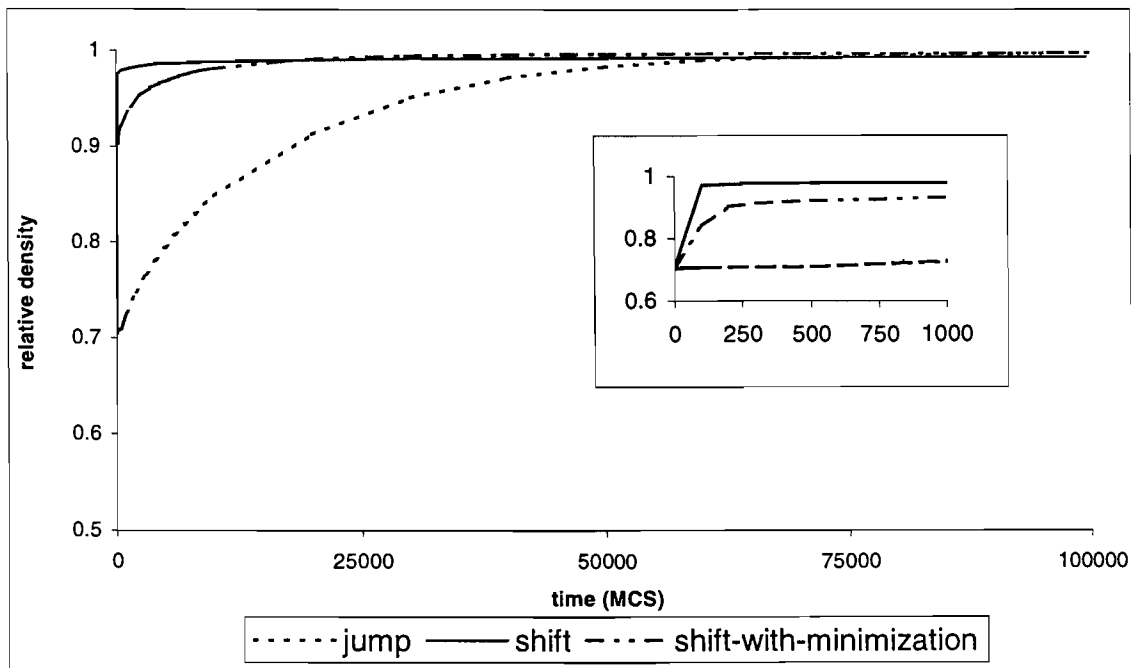
Figure 5. Densification curves for different algorithms starting from a random initial configuration

30

(A) Jump algorithm
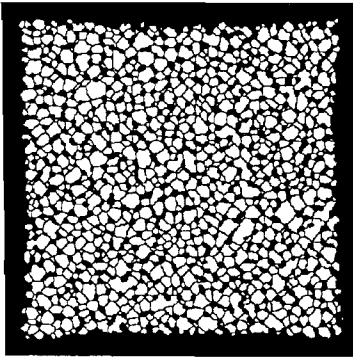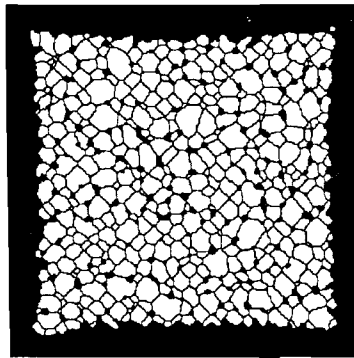
| after 10^4 MCS | after 3×10^4 MCS | after 10^5 MCS |
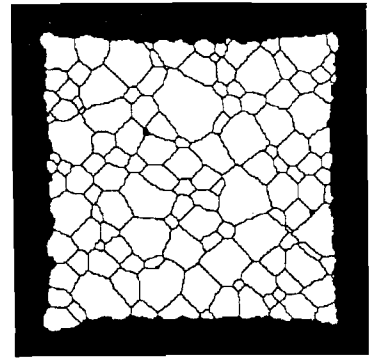
(B) Shift algorithm
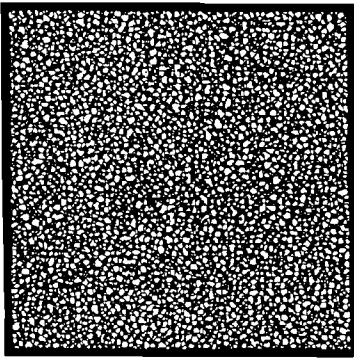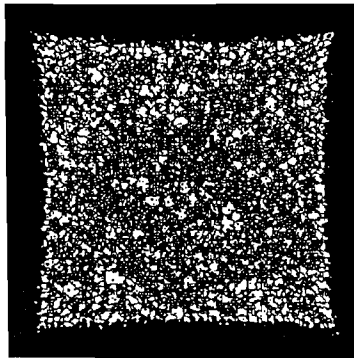
| after 500 MCS | after 800 MCS | after 10^3 MCS |
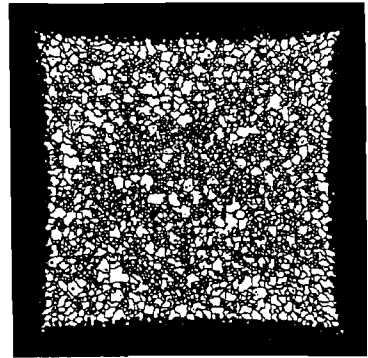
(C) Shift-with-minimization algorithm
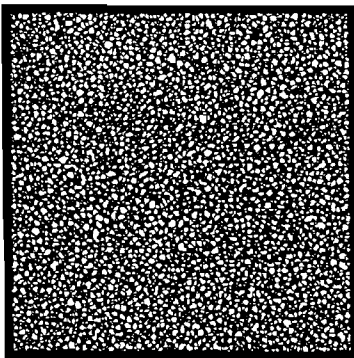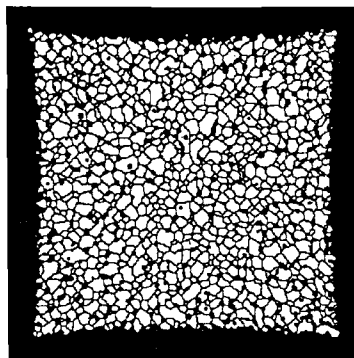
| after 500 MCS | after 2×10^3 MCS | after 2×10^4 MCS |
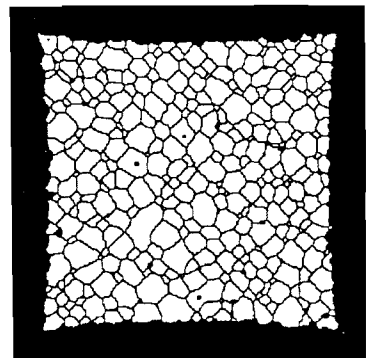
Figure 6. Microstructures obtained using the different algorithms from a randomly packed non-uniform powder
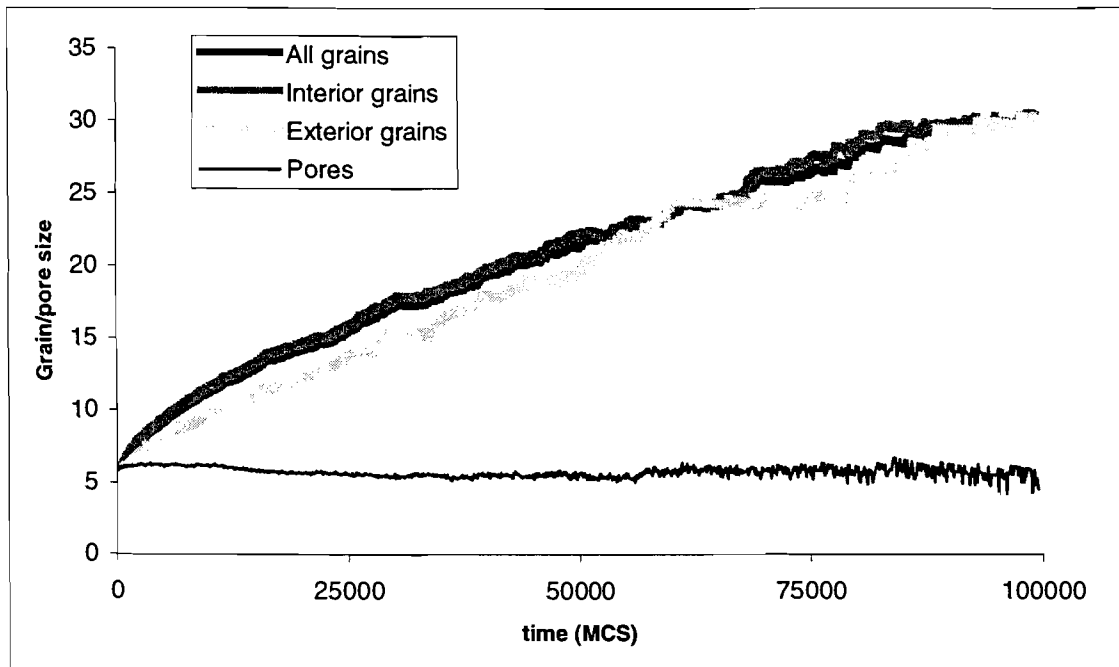
Figure 7. Grain and pore size statistics for densification from random configuration in the jump algorithm. Average sizes are shown as function of time (in MCS).

In addition, the number of exterior grains is much smaller than the number of interior grains in these simulations. Therefore, the overall grain statistics is affected only insignificantly. Note that the shift and the shift-with-minimization algorithms alter grain size statistics very substantially.

Discussion and conclusions

Similar to other areas of Materials Science, modeling of sintering comprises two distinct approaches: microstructural mesoscopic models and macroscopic continuum models. Despite the significant progress achieved in understanding microstructural processes of sintering, the connection between the micro- and macro- structural models is still approximated by phenomenological constitutive relations based on highly idealized geometries. The latter statement is true not just for the current state of sintering modeling, but also for the state of simulation of a wide range of different phenomena for which macrostructural evolution is determined, at least in part, by microstructural rearrangements. The problem is that macroscopic behavior, while dependent on the underlying local interaction mechanisms, is controlled by the whole set of local interactions, i.e., by collective microstructural phenomena.

Until recently, simulation of microstructural evolution of large systems was not feasible due to the computer power limitations. It is becoming increasingly possible to simulate microstructural behavior of large systems, and this development is paving the way for

embedding microstructural evolution into macroscopic models. For instance, in dislocation-based plasticity modeling only in the late 90s did it become viable to directly calculate interactions of large numbers of dislocations [31-33], which in turn allowed plasticity models to move beyond continuum phenomenological theories that rely on field quantities to approximate collective microstructural phenomena [34-40].

In the modeling of sintering the need for the incorporation of mesoscopic simulations into macroscopic models is even greater because microstructural evolution provides the driving force for macroscopic deformation in sintering. Therefore, a mesoscopic model of sintering capable of simulating large powder compacts could be a step to more realistic macroscopic models. We discuss these aspects of our work elsewhere [41], but it is important to state the requirements a model should satisfy for this development to be possible.

First of all, the model should not have any a priori geometric assumptions. Second, the model should not rely on semi-arbitrary division of the sintering process into stages, relying on more local, basic physical processes. The problem with the stages – and most current sintering models have 2 or 3 stages – is that there are no exact points when one stage ends and the next begins because the distinction between the stages is based on overall or average characteristics of the compact. Consider, for instance, Ashby's model [25] that distinguishes two stages of sintering (microstructures with open and closed porosity) with different densification laws. Density is used as the criterion for considering the compact in one or the other stage in this model, with the second stage starting at 0.92 of the theoretical density of the compact. The number is based on consideration of a powder compact with spherical particles and, thus, incorporates geometric assumptions. Other models use similar approaches to criteria dividing the process of sintering into stages. And, finally, the model, as mentioned above, should be scalable, i.e., it should be able to simulate large powder compacts.

The simulation technique we present satisfies all three requirements. The model does not need any geometric assumptions because the microstructural development is simulated in it based on a set of simple *local* rules and overall thermodynamic laws. The state of each pixel depends only on the state of its neighboring pixels, not on the state of the whole system at each point in time. Thus, the system can exhibit the open and closed porosity stages as seen in microstructures in figure 6 for the second example in 3.1, but the model does not require any a priori information on those stages or any change in the simulation rules when the porosity becomes closed. The Potts model, which is the basis of our sintering model, has been shown to be scalable [15-18]. The addition of the annihilation mechanism, understandably, slows the calculation, but not very significantly and does not require more memory usage. Therefore, the third requirement is satisfied also.

Consider now the three different algorithms of incorporating annihilation into the kinetic Monte-Carlo (Potts) model discussed in 3. While there were rather significant differences when these routines were applied in numerical experiments with random initial configurations, the differences in the numerical results for packed 2D configurations were much less prominent as shown by the results discussed in 3.1. The shift algorithms that tend to lead to unphysical results for random starting configurations are, in addition, significantly more computationally complex requiring more computer time. The small artifact that the jump algorithm introduces – namely,

the difference in average grain size between the exterior and interior grains due to the annihilation procedure – is not significant because the rate of grain growth is much higher than the rate of artificial shrinkage of the exterior grains. In addition, being a boundary effect, this artifact becomes less and less important with the increase of the simulation size. Therefore, we chose the jump algorithm as the basis for further development.

There is another important characteristic of the model that we need to address: by moving porosity to the boundary regions, the procedure homogenizes the deformation of the simulation area. This feature might be even conducive for the connection to macroscopic continuum models, which require some average, or homogenized, information from the microstructures, but because of it the algorithm does not allow for the defect growth that occurs in many materials during sintering. The algorithm does allow for modifications, like jumps to defects in addition to the jumps to the boundary of the compact, which can simulate the defect growth. This issue together with the generalization to 3D,that is usually straightforward for kinetic Monte-Carlo algorithms, will be the focus of the further development of the model.

References

[1]   P. Zeng, S. Zajac, P.C. Clapp, J.A. Rifkin, "Nanoparticle sintering simulations," Mater. Sci. Eng. A, **252** [2] 301-306 (1998).

[2]   J. Pan, H. Le, S. Kucherenko, J.A. Yeomans," A model for the sintering of spherical particles of different sizes by solid state diffusion," Acta Mater., **46** [13], 4671-4690 (1998).

[3]   H. Zhou and J.J. Derby, "Three-dimensional finite-element analysis of viscous sintering ," J. Am. Ceram. Soc., **81**, [3] 533-540 (1998).

[4]   J.W. Bullard, "Digital-image-based models of two-dimensional microstructural evolution by surface diffusion and vapor transport," J. Appl. Phys., **81** [1] 159 -168 (1997).

[5]   W. Zhang, J.H. Scheibel, "The sintering of 2 particles by surface and grain-boundary diffusion : a 2-dimensional numerical study ," Acta Metall. Mater., **43** [12] 4377-4386 (1995).

[6]   A. Jagota, P.R. Dawson, "Micromechanical modeling of powder compacts .1. Unit problems for sintering and traction induced deformation," Acta Metall. Mater., **36** [9] 2551-2561 (1988).

[7]   Y.E. Geguzin, Physics of sintering, 2nd edition, Nauka, Moscow (1984) (in Russian)

[8]   G.C Kuczynski, J. Appl. Phys. 21, 632 (1950);

[9]   W.D. Kingery and M. Berg, J. Appl. Phys. 26, 1205 (1955);

[10]   R.L. Coble, J. Am. Ceram. Soc., 41, 55 (1958);

[11]   D.L. Johnson J. Appl. Phys. 40, 192 (1969);

[12]   M.F. Ashby, Acta Metall. Mater., 22 275 (1974)

[13]   E.A. Olevsky, "Theory of sintering: from discrete to continuum ," Mater. Sci. Eng. R, **23** [2] 41-100 (1998).

[14]   V.V. Skorohod, Reological basis of the theory of sintering, Naukova Dumka, Kiev (1972);

[15]   F. Y. Wu , "The Potts-model," Rev. Modern Phys., **54** [1] 235-268 (1982).

[16]   M.P. Anderson, D.J. Srolovitz, G.S. Grest, and P.S. Sahni, "Computer-simulation of grain-growth .1. Kinetics, " Acta Metall. Mater., **32** [5] 783-791 (1984).

[17]   J. Wejchert, D. Weaire, J.P. Kermode, "On the distribution of cell areas in a Voronoi network ," Philos. Mag. B, 53 [5] L101-L105 (1986).

[18]   E.A. Holm, James A. Glazier, D.J. Srolovitz, G.S. Grest, "Effects of lattice anisotropy and temperature on domain growth in the 2-dimensional Potts-model ," Phys. Rev. A, **43** [6] 2662-2668 (1991).

[19]   R.T. DeHoff, "Stereological Theory of Sintering," *Science of Sintering* ed. by D.P. Uskokovic et al, 55-71, Plenum Press, New York (1989)

[20]   G.N. Hassold, I-W, Chen, D.J. Srolovitz, "Computer-simulation of final-stage sintering. 1. Model, kinetics, and microstructure," J. Am. Ceram. Soc., **73** [10] 2857-2864 (1990).

[21]   V. Tikare and E.A. Holm, "Simulation of grain growth and pore migration in a thermal gradient," J. Am. Ceram. Soc., **81**[3] 480-484 (1998).

[22]   V. Tikare and J.D. Cawley, "Application of the Potts model to simulation of Ostwald ripening ," J. Am. Ceram. Soc., **81** [3] 485-491 (1998).

[23]   W. Horsthemke and R. Lefever, Noise-induced transitions: theory and applications in physics, chemistry, and biology , Berlin ; New York : Springer-Verlag, 1984.

[24]   C. Truesdell, Rational thermodynamics; a course of lectures on selected topics, New York, McGraw-Hill, 1969

[25]   M.F. Ashby, Background reading, HIP6.0, University of Cambridge, UK, 1990

[26]   E. Arzt, "The influence of an increasing particle coordination on the densification of spherical powders," Acta Metall. Mater., **30** [10] 1883-1890 (1982).

[27]   H.F. Fischmeister, E. Arzt and L.R. Olsson, "Particle deformation and sliding during compaction of spherical powders: study by quantitative metallography ," Powder Metall., **21** [4] 179-187 (1978).

[28]   H.F. Fischmeister and E. Arzt, "Densification of powders by particle deformation," Powder Metall., **26** [2] 82-88 (1983).

[29] A.S. Helle, K.E. Easterling and M.F. Ashby, "Hot-isostatic pressing diagrams: new developments," Acta Metall. Mater., **26** [12] 2163- 2174 (1985)

[30] B.H. Alexander and R.W. Balluffi, "The Mechanism of Sintering of Copper," Acta Metall. Mater., **5** 666-677 (1957)

[31] Schwarz K.W., "Simulation Of Dislocations On The Mesoscopic Scale :I: Methods And Examples," J. Appl. Phys., **85** [1] 108-119 (1999)

[32] Needleman A, Van Der Giessen E., "Discrete Dislocation And Continuum Descriptions Of Plastic Flow," Mater. Sci. Eng. A, **309** (SISI) 1-13 (2001)

[33] Devincre B., Kubin L.P., Lemarchand C., Madec R., "Mesoscopic Simulations Of Plastic Deformation," Mater. Sci. Eng. A, **309** (SISI) 211-219 (2001)

[34] Walgraef D., Aifantis E.C., "Plastic Instabilities, Dislocation Patterns And Nonequilibrium Phenomena," Res Mechanica, **23** [2-3] 161-195 (1988)

[35] Kubin L.P., Estrin Y., "Evolution Of Dislocation Densities And The Critical Conditions For The Portevin-Lechatelier Effect," Acta Metall. Mater., **38** [5] 697-708 (1990)

[36] Ananthakrishna G., "Formation, Propagation Of Bands And Chaos In Jerky Flow," Scripta Metall. Mater , **29** [9] 1183-1188 (1993)

[37] Estrin Y., Kubin L.P., "Plastic Instabilities: Phenomenology And Theory," Mater. Sci. Eng. A, **137** 125-134 (1991)

[38] Kubin L.P., Canova G., "The Modeling Of Dislocation Patterns," Scripta Metall. Mater., **27** [8] 957-962 (1992)

[39] Estrin Y., Kubin L.P., Aifantis E.C., "Introductory-Remarks To The Viewpoint Set On Propagative Plastic Instabilities," Scripta Metall. Mater., **29** [9] 1147-1150 (1993)

[40] Glazov M.V., Laird C., "Size Effects Of Dislocation Patterning In Fatigued Metals," Acta Metall. Mater., **43** [7] 2849-2857 (1995)

[41] Tikare V., Braginsky M., Olevsky E., "An integrated study of sintering at two different hierarchial levels of structure. Part II: Meso-scale modeling and determination of constitutive parameters." Submitted for publication in the J. Am. Ceram. Soc.

Chapter 4

Connecting Microstructural Evolution and Macroscopic Constitutive Models

Michael Braginsky

The continuum theory of sintering has been developed to describe macroscopic shrinkage and deformation in a sintering body. This theory condenses all the microstructural changes during sintering into a few continuum thermodynamic and kinetic quantities that are used to describe the shrinkage during sintering. The main constitutive relationship of the *isotropic* continuum theory of sintering[1] is:

$$\sigma_{ij} = \frac{\sigma(W)}{W}\left[\varphi\dot{\varepsilon}_{ij} + \left(\psi - \frac{1}{3}\varphi\right)\dot{e}\delta_{ij}\right] + P^L\delta_{ij} \qquad \text{Eq. (1)}$$

where φ and ψ are the normalized shear and bulk viscosity moduli. They are functions of microstructural parameters such as porosity θ, grain shape and size, interparticle neck geometry, etc. δ_{ij} is the Kronecker delta; $\dot{e}$ is the first invariant of the strain rate tensor $\dot{\varepsilon}$. Physically, $\dot{e}$ represents the volume change rate of a porous body or shrinkage rate. The effective equivalent strain rate W is a function of the instantaneous porosity and the invariants of the strain rate tensor. The effective equivalent stress $\sigma(W)$ determines the constitutive behavior of a porous material. P^L is the effective Laplace stress (macroscopic sintering pressure), which depends on the local sintering pressure P^{lo}, (sintering pressure in the immediate microstructural environment), porosity and various pore structure parameters such as relative interparticle neck radius. θ is the relative porosity calculated as the ratio of pore volume to volume of the porous body.

A more general, anisotropic, nonlinear constitutive relationship can be written as

$$\sigma_{ij} = F_{ij}\left(\dot{\varepsilon}_{kl}\right) + P_{ij}^L \qquad \text{Eq. (2)}$$

where $F_{ij}\left(\dot{\varepsilon}_{ij}\right)$ is some non-linear tensor function (functional) depending on the strain rate. In the linear anisotropic case reduces to

$$\sigma_{ij} = A_{ijkl}\dot{\varepsilon}_{kl} + P_{ij}^L \qquad \text{Eq. (3)}$$

with A_{ij} denoting the tensor of viscous properties. The effective Laplace stress P_{ij}^L in both (2) and (3) is not a scalar representing a hydrostatic tensor as in (1), but a tensor quantity.

We would like to be able to determine parameters of the constitutive models – especially, the sintering stress – from microstructural simulations. Below we discuss ways to achieve this goal. Since there are, as discussed in the following, very significant differences between the isotropic and anisotropic cases, these two cases are considered separately starting with the isotropic case, which is simpler.

Isotropic sintering

In the framework of the continuum theory of sintering, the effective Laplace pressure (sintering stress) P^L is defined based on thermodynamics as follows[1].

Considering the Helmholz free energy of the form

$$F = F(T, \vartheta)$$
Eq. (4)

where T denotes temperature, and ϑ is the specific volume, and the second law of thermodynamics in the form

$$\sigma_{ij}\dot{\varepsilon}_{ij} - \rho\dot{F} - \rho S\dot{T} \geq 0$$
Eq. (5)

(with no heat flux), one obtains by substituting into (5) the time derivative of (4):

$$\left(\sigma_{ij} - \frac{\partial F}{\partial \vartheta}\delta_{ij}\right)\dot{\varepsilon}_{ij} - \rho\left(\frac{\partial F}{\partial T} + S\right)\dot{T} \geq 0,$$
Eq. (6)

which leads to the identification of the Laplace pressure as

$$P^L = \frac{\partial F}{\partial \vartheta}\bigg|_T$$
Eq. (7)

Relationship (7) can be used to directly calculate the effective sintering stress from microstructural simulations. The part of the free energy that corresponds to mechanical deformation is identified as the energy associated with the free surface area. At each step of the microstructure evolution the shrinking volume and the free surface of the grain-pore arrangement are calculated. Then, numerical differentiation is performed to determine the effective sintering stress. In order to stabilize the numerical differentiation, we use a regularization procedure.

Having found the effective sintering stress, we can use simulation data together with (1) to determine the normalized effective bulk viscosity modulus, ψ. Indeed, for free sintering that is studied in our microstructural simulations, (1) is reduced to

$$P^L = -\frac{\sigma(W)}{W}\psi\dot{e}$$
Eq. (8)

which allows the determination of ψ from the known effective sintering stress[iii]

Notice, that microstructural simulations of free sintering leave the normalized shear viscosity modulus, φ, indeterminate because deformation during free sintering in the isotropic case is hydrostatic, which is manifested by the fact that φ does not appear in (8). The shear viscosity modulus could be determined from sinter forging, i.e., the simulations incorporating applied stresses, not just free sintering.

Anisotropic sintering

In the anisotropic case the total macroscopic deformation of a sample is not characterized by the changes in volume only. In the case of simple stretching along principal axes, the free energy has to be a function of temperature and the macroscopic (uniform) deformation tensor.

$$F = F(T, \varepsilon)$$
Eq. (9)

[iii] The effective equivalent strain rate W, the effective equivalent stress $\sigma(W)$, and the first invariant of the strain rate tensor, $\dot{e}$, are, of course, known through the simulation.

The free energy can be written as function of invariants of the strain tensor, e.g., its principal values.

While a function of invariants of a tensor is an isotropic function of that tensor, i.e., it is not dependent on the rotations of that tensor, the use of form (9) for the description of anisotropic sintering is justified. Indeed, when we are talking of anisotropic sintering, we mean that the sintering stress is no longer *hydrostatic*, as in the isotropic case. All we state assuming the form (9) is that the sintering stress defined as a derivative of such an isotropic function with respect to the macroscopic strain is affine to that strain, i.e., the **connection** between the sintering stress and the macroscopic sintering strain is **isotropic**. The shrinkage due to the non-hydrostatic sintering stress will not be isotropic.

Constructing a more complicated free energy function proves problematic. To do that, we must include other tensors or vectors, thus increasing the number of invariants the function can depend upon, because free energy has to be represented by isotropic functions[iv]. For instance, a free energy function for a transversely isotropic material will be an isotropic function of the form F=F(**E**, **nn**), where **E** stands for the macroscopic strain tensor, while **n** is the symmetry direction. The invariants that F can depend upon include in addition to the invariants of **E** also **nn:E** and tr(**E*E*nn**)^2. This implies that symmetry information has to come from somewhere, i.e., we need some a priori information about viscous properties, which is not available. If we were to assume that the symmetry direction **n** corresponds to a principal vector of the strain tensor (which is exactly the case in our computer experiments), the formulation would reduce right away to (9), since in this case the more complicated free energy function reduces to an isotropic function of the principal values of the macroscopic strain and, hence, of any 3 invariants of the macroscopic strain we would like to choose.

Following the same procedure (4) – (7) we get for the 2-nd Law of thermodynamics:

$$\sigma_{ij}\dot{\varepsilon}_{ij} - \rho\frac{\partial F}{\partial \varepsilon_{ij}}\dot{\varepsilon}_{ij} - \rho\left(\frac{\partial F}{\partial T}+S\right)\dot{T} \geq 0 \qquad \text{Eq. (10)}$$

and obtain from (10)

$$\left(\sigma_{ij} - \rho\frac{\partial F}{\partial \varepsilon_{ij}}\right)\dot{\varepsilon}_{ij} - \rho\left(\frac{\partial F}{\partial T}+S\right)\dot{T} \geq 0 \qquad \text{Eq. (11)}$$

which rigorously identifies the anisotropic 'Laplace pressure' as:

$$P_{ij}^{L} = \rho\frac{\partial F}{\partial \varepsilon_{ij}} \qquad \text{Eq. (12)}$$

Notice that if the free energy depends on volume only, (9) may be written as

$$F = F(T, I_1), \qquad \text{Eq. (13)}$$

[iv] **otherwise it won't be a scalar**

39

where[v] $I_1 \equiv \varepsilon_{ii}$ is the first invariant of the macroscopic strain tensor. With the substitution of (13), (11) becomes

$$\sigma_{ij}\dot{\varepsilon}_{ij} - \rho\frac{\partial F}{\partial I_1}\dot{\varepsilon}_{ij}\delta_{ij} - \rho\left(\frac{\partial F}{\partial T} + S\right)\dot{T} \geq 0,$$

which, obviously, recovers (7) since from

$$\frac{\dot{V}}{V} = \dot{I}_1 \qquad\qquad \text{Eq. (14)}$$

we find that

$$V = V_0 \exp(I_1) \qquad\qquad \text{Eq. (15)}$$

where V_0 is the initial (undeformed) volume; this means that

$$\frac{\partial F}{\partial I_1} \equiv \frac{\partial F}{\partial V}\cdot\frac{\partial V}{\partial I_1} = V\frac{\partial F}{\partial V} \qquad\qquad \text{Eq. (16)}$$

because from (15) $\dfrac{dV}{dI_1} = V$; Since $\vartheta = \dfrac{1}{\rho}$

$$\rho V\frac{\partial F}{\partial V} \equiv \frac{\partial F}{\partial\vartheta} \qquad\qquad \text{Eq. (17)}$$

To study the connection between the anisotropic formulation and the classic formulation of (1) – (4), we can further specify the free energy function (9) as.

$$F = F(T, I_1, J_2, J_3), \qquad\qquad \text{Eq. (18)}$$

where J_2 and J_3 are the invariants of the deviatoric part of the macroscopic strain tensor. These three invariants determine the deformation tensor completely. The choice of the second and third invariants of the *deviatoric* part of the tensor and not of the strain tensor itself is made specifically to avoid additional terms in the hydrostatic part of the sintering stress, since derivatives with respect to a deviatoric part of a tensor are independent of the hydrostatic part of the same tensor and vice versa[vi]. In the principal axes of strain $\{\varepsilon_x, \varepsilon_y, \varepsilon_z\}$ these invariants are:

$$J_2 = \left(2\varepsilon_x - \varepsilon_y - \varepsilon_z\right)^2 + \left(2\varepsilon_y - \varepsilon_x - \varepsilon_z\right)^2 + \left(2\varepsilon_z - \varepsilon_y - \varepsilon_x\right)^2$$
$$J_3 = \left(2\varepsilon_x - \varepsilon_y - \varepsilon_z\right)\cdot\left(2\varepsilon_y - \varepsilon_x - \varepsilon_z\right)\cdot\left(2\varepsilon_z - \varepsilon_y - \varepsilon_x\right)$$

Eq. (19)

coefficients of 1/3 and 1/9 are omitted in J_2 and J_3, respectively, as irrelevant.

---

[v] **summation in a repeating index is implied**
[vi] **what happens if we consider the free energy as a function of the invariants of the strain tensor itself is shown in the Appendix 2.**

Substitution of (18) into (12) results in the following principal values of the sintering stress tensor $\left\{ P_x^L, P_y^L, P_z^L \right\}$:

$$P_x^L = \rho \frac{\partial F}{\partial \varepsilon_x} = \rho \left[\frac{\partial F}{\partial I_1} + 6 \frac{\partial F}{\partial J_2} \cdot \left(2\varepsilon_x - \varepsilon_y - \varepsilon_z \right) + \frac{\partial F}{\partial J_3} \cdot \frac{\partial J_3}{\partial \varepsilon_x} \right];$$

$$P_y^L = \rho \frac{\partial F}{\partial \varepsilon_y} = \rho \left[\frac{\partial F}{\partial I_1} + 6 \frac{\partial F}{\partial J_2} \cdot \left(2\varepsilon_y - \varepsilon_x - \varepsilon_z \right) + \frac{\partial F}{\partial J_3} \cdot \frac{\partial J_3}{\partial \varepsilon_y} \right]; \qquad \text{Eq. (20)}$$

$$P_z^L = \rho \frac{\partial F}{\partial \varepsilon_z} = \rho \left[\frac{\partial F}{\partial I_1} + 6 \frac{\partial F}{\partial J_2} \cdot \left(2\varepsilon_z - \varepsilon_y - \varepsilon_x \right) + \frac{\partial F}{\partial J_3} \cdot \frac{\partial J_3}{\partial \varepsilon_z} \right].$$

Here we used the fact the first invariant of the deviatoric part is zero. Derivatives of J_3 with respect to principal strains are given in the Appendix 1 (equation (31)); they are not shown in (20) because the expressions are too long.

It is shown in the Appendix 1 that the first invariant of the sintering stress tensor:

$$I_1^S = \frac{1}{3} \left(P_x^L + P_y^L + P_z^L \right) = \rho \frac{\partial F}{\partial I_1} = \frac{\partial F}{\partial \vartheta} \qquad \text{Eq. (21)}$$

which coincides with the formula for the isotropic case. In the Appendix 2 it is shown that if the free energy is considered as a function of the invariants of the strain tensor itself, not in the form of (9), the formula for the first invariant of the sintering stress is more complicated.

As was shown above, the thermodynamic approach works nicely in the isotropic case allowing to determine both the sintering stress (7) and the normalized effective bulk viscosity modulus (8). Unfortunately, we were not able to generalize this approach to the anisotropic case.

Consider the determination of the sintering stress from (12), or, in principal components, from (20). Unlike the expression for the isotropic case which involved only the derivative of the free energy with respect to the first invariant of the strain tensor (7). Consider, for instance, the expression for the P_x^L:

$$P_x^L = \rho \frac{\partial F}{\partial \varepsilon_x} = \rho \left[\frac{\partial F}{\partial I_1} + 6 \frac{\partial F}{\partial J_2} \cdot \left(2\varepsilon_x - \varepsilon_y - \varepsilon_z \right) + \frac{\partial F}{\partial J_3} \cdot \frac{\partial J_3}{\partial \varepsilon_x} \right] \qquad \text{Eq. (22)}$$

In the simulation we do know the time dependencies of $F, \varepsilon_x, \varepsilon_y, \varepsilon_z, I_1, J_2, J_3$, and any other geometric characteristic we would like to calculate. But the problem is that they do not vary independently. The derivatives that we can calculate are not partial, but full time derivatives. And we have just one equation to determine the three unknown partial derivatives:

$$\frac{dF}{dt} = \frac{\partial F}{\partial I_1} \frac{dI_1}{dt} + \frac{\partial F}{\partial J_2} \frac{dJ_2}{dt} + \frac{\partial F}{\partial J_3} \frac{dJ_3}{dt} \qquad \text{Eq. (23)}$$

There are not enough equations to determine all three partial derivatives and, thus, the sintering stress. The only reason this approach works in the isotropic case is that there we need just one derivative (7), which relates nicely to the full time derivative. In the anisotropic case this can work with some additional assumptions on the relationship of different components of sintering stress. Such assumptions, though, are as unjustifiable as they are undesirable.

A more promising approach, that seems to be working[vii] is to abandon the free energy connection to the sintering stress altogether, and to find the viscous moduli – only the components relevant for the free sintering – from the dissipative potential.

Consider an anisotropic viscous model (3)[viii]

$$\sigma_{ij} - P_{ij}^L = A_{ijkl}\dot{\varepsilon}_{kl} ,$$
<div align="right">Eq. (24)</div>

that for free sintering reduces to

$$-P_{ij}^L = A_{ijkl}\dot{\varepsilon}_{kl} ,$$
<div align="right">Eq. (25)</div>

The energy dissipation rate that is determined as the contraction of stress with the strain rate is

$$\dot{F} = P_{ij}^L \dot{\varepsilon}_{ij} = -A_{ijkl}\dot{\varepsilon}_{ij}\dot{\varepsilon}_{kl}$$
<div align="right">Eq. (26)</div>

Integrating (26), obtain

$$\Delta F = -\int_{t_0}^{t_1} A_{ijkl}\dot{\varepsilon}_{ij}\dot{\varepsilon}_{kl} dt$$
<div align="right">Eq. (27)</div>

If the viscous moduli are constant on some interval (27) is reduced to

$$\Delta F = -A_{ijkl}\int_{t_0}^{t_1}\dot{\varepsilon}_{ij}\dot{\varepsilon}_{kl} dt$$
<div align="right">Eq. (28)</div>

which can be used for approximating the real non-linear dependence of the viscous moduli on microstructural parameters by piecewise constant functions. Assuming that we can have enough points inside the interval $\left[t_0, t_1\right]$ that we can form as many equations as needed to calculate all the required components of the moduli tensor[ix], we can then determine the sintering stress from (25).

Consider the implementation of this methodology in 2D.

[vii] **We are working on the verification of this methodology, but this work has not been completed yet**

[viii] **Here A_{ijkl} can be viewed as a function of time, strain, etc; therefore, the model is non-linear.**

[ix] **It is beneficial for the stability of the method to have the systems with more equations than there are unknowns and to use the least-squares method to determine the unknowns.**

The strain tensor has only two principal components ε_{11} and ε_{22}. Since all the other components of strain in our simulation are zero, the only components of the viscous moduli tensor of interest are A_{1111}, A_{1122}, and A_{2222}.[x]

The calculation would proceed as follows:

1) Assign two time lengths: δt, the length of the time segment, and dt, the subsegment. It is assumed that we can consider the viscous moduli tensor constant on any segment of the length δt.

2) Start at t_0. Form equations based on (28) as follows:

$$\Delta F_i = -A_{1111} \int_{t_i}^{t_{i+1}} \dot{\varepsilon}_{11}\dot{\varepsilon}_{11}dt - 2A_{1122} \int_{t_i}^{t_{i+1}} \dot{\varepsilon}_{11}\dot{\varepsilon}_{22}dt - A_{2222} \int_{t_i}^{t_{i+1}} \dot{\varepsilon}_{22}\dot{\varepsilon}_{22}dt \qquad \text{Eq. (29)}$$

where $t_i = t_0 + i \cdot dt$; for all $i \in \left[0, Int\left(\dfrac{\delta t}{dt}\right)\right]$;

It is obvious that, at the very least, 3 equations are needed, but an overdetermined system would be much more stable.

- It is important to check whether ΔF_i is, indeed, negative. Microstructural simulation allows energy to increase at times, while this cannot happen in the macroscopic model. Thus, leaving non-negative ΔF_i will lead to non-physical results, such as negative viscous coefficients.

- Negative viscous coefficients appear sometimes even when all non-negative ΔF_i are left out. This seems to indicate, as in the case of isotropic sintering considered under this framework, that A_{1122} is vanishing. In such a case we set $A_{1122} = 0$ and form the system (29) with this assumption. The coefficients A_{1111} and A_{2222} determined from this new system were in all cases positive.

3) Solve the system formed by (29) using singular value decomposition.
4) Calculate the sintering stress using (25) based on this solution
5) Set $t_0 = t_0 + dt$ and go back to step 2 [xi].

Thus, the procedure allows for changes in viscous properties with time under the assumption that this change is much slower than the time scale δt.

Appendix 1. Derivation of equation (21)

---

[x] $A_{2211} = A_{1122}$
[xi] **The procedure, of course, has to be organized effectively as to not calculate the same integrals several times.**

$$I_1^S = \frac{1}{3}\left(P_x^L + P_y^L + P_z^L\right) = \rho\frac{\partial F}{\partial I_1} + \frac{1}{3}\rho\frac{\partial F}{\partial J_3}\cdot\left[\frac{\partial J_3}{\partial \varepsilon_x} + \frac{\partial J_3}{\partial \varepsilon_y} + \frac{\partial J_3}{\partial \varepsilon_z}\right] +$$

$$+2\rho\frac{\partial F}{\partial J_2}\cdot\left[\left(2\varepsilon_x - \varepsilon_y - \varepsilon_z\right) + \left(2\varepsilon_y - \varepsilon_x - \varepsilon_z\right) + \left(2\varepsilon_z - \varepsilon_y - \varepsilon_x\right)\right]$$

Eq. (30)

The coefficient of $\dfrac{\partial F}{\partial J_2}$ is zero because it is the first invariant of the deviatoric part of the strain tensor. It is a little bit more involved to show that the coefficient of $\dfrac{\partial F}{\partial J_3}$ is also zero.

$$\frac{\partial J_3}{\partial \varepsilon_x} = 2\left(2\varepsilon_y - \varepsilon_x - \varepsilon_z\right)\left(2\varepsilon_z - \varepsilon_y - \varepsilon_x\right) + \left(2\varepsilon_x - \varepsilon_y - \varepsilon_z\right)^2 ;$$

$$\frac{\partial J_3}{\partial \varepsilon_y} = 2\left(2\varepsilon_z - \varepsilon_x - \varepsilon_y\right)\left(2\varepsilon_x - \varepsilon_y - \varepsilon_z\right) + \left(2\varepsilon_y - \varepsilon_x - \varepsilon_z\right)^2 ; \qquad \text{Eq. (31)}$$

$$\frac{\partial J_3}{\partial \varepsilon_z} = 2\left(2\varepsilon_y - \varepsilon_x - \varepsilon_z\right)\left(2\varepsilon_x - \varepsilon_y - \varepsilon_z\right) + \left(2\varepsilon_z - \varepsilon_y - \varepsilon_x\right)^2$$

$$\frac{\partial J_3}{\partial \varepsilon_x} + \frac{\partial J_3}{\partial \varepsilon_y} + \frac{\partial J_3}{\partial \varepsilon_z} = \left(2\varepsilon_x - \varepsilon_y - \varepsilon_z\right)^2 + \left(2\varepsilon_y - \varepsilon_x - \varepsilon_z\right)^2 + \left(2\varepsilon_z - \varepsilon_x - \varepsilon_y\right)^2 +$$

$$+2\left(2\varepsilon_y - \varepsilon_x - \varepsilon_z\right)\left(2\varepsilon_z - \varepsilon_y - \varepsilon_x\right) + 2\left(2\varepsilon_z - \varepsilon_x - \varepsilon_y\right)\left(2\varepsilon_x - \varepsilon_y - \varepsilon_z\right) +$$

$$+2\left(2\varepsilon_y - \varepsilon_x - \varepsilon_z\right)\left(2\varepsilon_x - \varepsilon_y - \varepsilon_z\right)$$

Eq. (32)

Consider

$$2\left(2\varepsilon_y - \varepsilon_x - \varepsilon_z\right)\left(2\varepsilon_z - \varepsilon_y - \varepsilon_x\right) + 2\left(2\varepsilon_z - \varepsilon_x - \varepsilon_y\right)\left(2\varepsilon_x - \varepsilon_y - \varepsilon_z\right) =$$

$$2\left(2\varepsilon_z - \varepsilon_y - \varepsilon_x\right)\left[\left(2\varepsilon_y - \varepsilon_x - \varepsilon_z\right) + \left(2\varepsilon_x - \varepsilon_y - \varepsilon_z\right)\right] = \qquad \text{Eq. (33)}$$

$$-2\left(2\varepsilon_z - \varepsilon_y - \varepsilon_x\right)^2$$

because $\left(2\varepsilon_y - \varepsilon_x - \varepsilon_z\right) + \left(2\varepsilon_x - \varepsilon_y - \varepsilon_z\right) + \left(2\varepsilon_z - \varepsilon_y - \varepsilon_x\right) = 0$

In the same manner we find that

$$\left(2\varepsilon_x - \varepsilon_y - \varepsilon_z\right)^2 + \left(2\varepsilon_y - \varepsilon_x - \varepsilon_z\right)^2 + \left(2\varepsilon_y - \varepsilon_x - \varepsilon_z\right)\left(2\varepsilon_x - \varepsilon_y - \varepsilon_z\right) = \left(2\varepsilon_z - \varepsilon_x - \varepsilon_y\right)^2 \text{ Eq. (34)}$$

Which, after substitution into (32) gives:

$$\frac{\partial J_3}{\partial \varepsilon_x} + \frac{\partial J_3}{\partial \varepsilon_y} + \frac{\partial J_3}{\partial \varepsilon_z} = \left(2\varepsilon_z - \varepsilon_x - \varepsilon_y\right)^2 + \left(2\varepsilon_z - \varepsilon_x - \varepsilon_y\right)^2 - 2\left(2\varepsilon_z - \varepsilon_x - \varepsilon_y\right)^2 \equiv 0 \qquad \text{Eq. (35)}$$

Thus from (30)

$$I_1^S = \frac{1}{3}\left(P_x^L + P_y^L + P_z^L\right) = \rho\frac{\partial F}{\partial I_1} = \frac{\partial F}{\partial \vartheta} \qquad \text{Eq. (36)}$$

The last equality of (36) has been established earlier in equations (14) - (17).

Appendix 2. Free energy as a function of the invariants of the strain tensor.

Consider now what happens if the free energy is considered a function of the invariants of the macroscopic tensor itself. Let

$$F = F\left(T, I_1, J_2, J_3\right) = \Psi\left(T, I_1, I_2, I_3\right), \qquad \text{Eq. (37)}$$

where I_2, I_3 are the second and third invariants of the macroscopic strain, respectively. In the principal strains they are:

$$I_2 = \varepsilon_x\varepsilon_y + \varepsilon_y\varepsilon_z + \varepsilon_x\varepsilon_z$$
$$I_3 = \varepsilon_x\varepsilon_y\varepsilon_z \qquad \text{Eq. (38)}$$

Substitution of (37) and (38) into (12) produces:

$$P_{Lx} = \rho\frac{\partial \Psi}{\partial \varepsilon_x} = \rho\left[\frac{\partial \Psi}{\partial I_1} + \frac{\partial \Psi}{\partial I_2}\cdot\left(\varepsilon_y + \varepsilon_z\right) + \frac{\partial \Psi}{\partial I_3}\cdot\varepsilon_y\varepsilon_z\right];$$

$$P_{Ly} = \rho\frac{\partial \Psi}{\partial \varepsilon_y} = \rho\left[\frac{\partial \Psi}{\partial I_1} + \frac{\partial \Psi}{\partial I_2}\cdot\left(\varepsilon_x + \varepsilon_z\right) + \frac{\partial \Psi}{\partial I_3}\cdot\varepsilon_x\varepsilon_z\right]; \qquad \text{Eq. (39)}$$

$$P_{Lz} = \rho\frac{\partial \Psi}{\partial \varepsilon_z} = \rho\left[\frac{\partial \Psi}{\partial I_1} + \frac{\partial \Psi}{\partial I_2}\cdot\left(\varepsilon_y + \varepsilon_x\right) + \frac{\partial \Psi}{\partial I_3}\cdot\varepsilon_x\varepsilon_y\right].$$

The first invariant of the stress tensor is now

$$I_1^S = \frac{1}{3}\left(P_{Lx} + P_{Ly} + P_{Lz}\right) =$$

$$= \rho\frac{\partial\Psi}{\partial I_1} + \frac{2}{3}\rho\frac{\partial\Psi}{\partial I_2}\left(\varepsilon_x + \varepsilon_y + \varepsilon_z\right) + \frac{1}{3}\rho\frac{\partial\Psi}{\partial I_3}\left(\varepsilon_x\varepsilon_y + \varepsilon_y\varepsilon_z + \varepsilon_x\varepsilon_z\right) = \qquad \text{Eq. (40)}$$

$$= \rho\frac{\partial\Psi}{\partial I_1} + \frac{2}{3}\rho\frac{\partial\Psi}{\partial I_2}I_1 + \frac{1}{3}\rho\frac{\partial\Psi}{\partial I_3}I_2 \equiv \frac{\partial\Psi}{\partial\vartheta} + \frac{2}{3}\rho\frac{\partial\Psi}{\partial I_2}I_1 + \frac{1}{3}\rho\frac{\partial\Psi}{\partial I_3}I_2$$

Thus, if the free energy is written not in the form (18), the hydrostatic part of the sintering pressure is not given just by the volume derivative of the free energy. This result was not unexpected, since while the hydrostatic and the deviatoric parts of a tensor are orthogonal (in the sense that their multiplication in both indices is zero), there are no such conditions for a hydrostatic part with any other parts of the same tensor.

References

[1] E. Olevsky, Theory of sintering: from discrete to continuum. Invited Review, *Mater. Sci. & Eng. R. Reviews*, 23, 41-100 (1998)
[2] Cemal Eringen, Mechanics of Continua (Appendix), R. E. Krieger Pub. Co., 1980, c1967, 2nd edition.

Chapter 5
Three-Dimensional Simulation of Sintering Using a Continuum Modeling Approach

J. G. Argüello, V. Tikare, T. J. Garino, M.V.Braginsky

Abstract

The continuum theory of sintering embodied in the constitutive description of Skorohod and Olevsky can be combined with results from mesostructure evolution simulations to model shrinkage and deformation of ceramics. The continuum portion is based on a finite element formulation that allows 3D components to be modeled using SNL's nonlinear large-deformation finite element code, JAS3D. This tool provides a capability to model sintering of complex three-dimensional components. The verification and performance of the implemented sintering constitutive model will be presented and discussed, as will the validation of the model using experimental results from various laboratory experiments performed by Garino.

1.0 Introduction

All ceramics and powder metals, including the ceramics components that Sandia National Laboratories (SNL) uses in various components such as PZT voltage bars and current stacks, multi-layer ceramic MET's, alumina/ molybdenum & alumina cermets, and ZnO varistors, are manufactured by sintering. Sintering is a critical, and possibly the most important, processing step during manufacturing of ceramics. The microstructural evolution, the macroscopic shrinkage, and shape distortions during sintering will control the engineering performance of the resulting ceramic component.

This paper describes the implementation, verification, and validation of a linear-viscous continuum model for sintering into SNL's Engineering Sciences Center nonlinear large-deformation finite element codes, specifically JAS3D. While the implemented model is a first order model in the sense that it handles only the linear-viscous case, it can be used as a basis for future work that might incorporate general nonlinear-viscous behavior, as well as one that can integrate the results of microstructural evolution of thousands of particles during sintering (Tikare & Braginsky, 2002) into the continuum description to predict the overall shrinkage and shape distortions in a sintering component. This phenomenological constitutive model will be referred to as the Skorohod-Olevsky Viscous Sintering (SOVS) constitutive model.

1.1 Skorohod-Olevsky Viscous Sintering Constitutive Relationship

An approach for macroscopically modeling the sintering process involves the use of continuum mechanics and is based on the theories of plastic and nonlinear-viscous deformation of porous bodies. An instance of this approach is embodied in a mathematical constitutive description developed by V. V. Skorohod (1972) and further advanced by E. A. Olevsky (1998). The result is a phenomenological constitutive model whereby a porous medium is considered as a two-phase material that includes a porous body skeleton phase and a void phase. The skeleton is assumed to be made-up of

individual particles having a general nonlinear-viscous incompressible isotropic behavior, and the voids are isotropically distributed. As a consequence, the overall response is isotropic.

The constitutive model described herein follows the formulation of the continuum theory of sintering of porous viscous materials as presented by Olevsky (1998). In the general case, the Skorohod-Olevsky viscous sintering (SOVS) constitutive relationship for a non-linear porous material can be written as:

$$\sigma_{ij} = \frac{\sigma(W)}{W}\left(\varphi\dot{\varepsilon}_{ij}' + \psi\dot{\varepsilon}_{kk}\delta_{ij}\right) + P_L\delta_{ij} \qquad \text{Eq. 1}$$

where σ_{ij} is the stress tensor; $\dot{\varepsilon}_{ij}$ is the strain rate tensor; $\dot{\varepsilon}_{ij}'$ is the deviatoric strain rate tensor; $\varphi = (1-\theta)^2 = \rho^2$; and $\psi = 2(1-\theta)^3/(3\theta) = 2\rho^3/\{3(1-\rho)\}$. In the foregoing, θ is the porosity of the material defined such that $\theta = 1-\rho$, where ρ is the relative density and $\rho = \rho_t/\rho_T$, with ρ_t being the density at any time t and ρ_T being the theoretical intact density of the material. P_L is the Laplace pressure or the sintering stress. Furthermore, $\sigma(W)$ is the "equivalent" stress and W is the "equivalent" strain.

1.2 The Linear Viscous Case

As a first step in developing a new capability at SNL for continuum modeling of sintering, it was decided that a linear-viscous approach would encompass much of the phenomenology seen in the materials of immediate interest for Sandia applications. The SOVS constitutive relationship for the <u>linear-viscous</u> porous case; i.e., $\sigma(W) = 2\eta_0 W$, can be written as, $\sigma_{ij} = (2\eta_0 W/W)(\varphi\dot{\varepsilon}_{ij}' + \psi\dot{\varepsilon}_{kk}\delta_{ij}) + P_L\delta_{ij}$ or,

$$\sigma_{ij} = 2\eta_0\varphi\dot{\varepsilon}_{ij}' + 2\eta_0\psi\dot{\varepsilon}_{kk}\delta_{ij} + P_L\delta_{ij}. \qquad \text{Eq. 2}$$

We can write the inverse relationship for this expression by recognizing that the stress consists of a deviatoric and a volumetric part. The inverse expression of Equation 2, with strain rate now a function of stress for the linear viscous case (adding a superscript, "$in.$", to indicate that this is the inelastic, i.e. viscous sintering, part of the total strain rate) can be written as:

$$\dot{\varepsilon}_{ij}^{in.} = \frac{\sigma_{ij}'}{2\eta_0\varphi} + \frac{(\sigma_{kk}/3 - P_L)}{3(2\eta_0\psi)}\delta_{ij}. \qquad \text{Eq. 3}$$

Equation 3 can be re-written in the more common form by recognizing that $\sigma_m = \sigma_{kk}/3$; $\sigma_s = P_L$; $\widetilde{G} = \eta_0\varphi$; and $\widetilde{K} = 2\eta_0\psi$ so that:

$$\dot{\varepsilon}_{ij}^{in.} = \frac{\sigma_{ij}'}{2\widetilde{G}} + \frac{(\sigma_m - \sigma_s)}{3\widetilde{K}}\delta_{ij} \qquad \text{Eq. 4}$$

with $\widetilde{G}$ being the effective shear viscosity and $\widetilde{K}$ being the effective bulk viscosity.

The elastic part of the material response is assumed to be isotropic and characterized by Hooke's Law as:

$$\dot{\sigma}_{ij} = C_{ijkl}\dot{\varepsilon}_{kl}^{el.}$$ Eq. 5

where C_{ijkl} is the elastic stiffness matrix and $\dot{\varepsilon}_{kl}^{el.}$ is the elastic strain rate. The total strain in the sintering body is given by:

$$\varepsilon_{kl}^{tot.} = \varepsilon_{kl}^{el.} + \varepsilon_{kl}^{in.} .$$ Eq. 6

Differentiating Equation 6 with respect to time and combining with Equation 5 gives the overall constitutive behavior as:

$$\dot{\sigma}_{ij} = C_{ijkl}(\dot{\varepsilon}_{kl}^{tot.} - \dot{\varepsilon}_{kl}^{in.})$$ Eq. 7

where $\dot{\varepsilon}_{kl}^{in.}$ is the inelastic, or sintering, portion of the strain rate given by Equation 3. The evolution of the relative density, ρ, is governed by mass conservation:

$$\dot{\theta}/(1-\theta) = \dot{\varepsilon}_{kk}^{in.} \text{ or } -\dot{\rho}/\rho = \dot{\varepsilon}_{kk}^{in.} .$$ Eq. 8

1.3 Integration of the Constitutive Model

A semi-implicit method described by McHugh and Riedel (1997) was used to integrate the system of coupled first order differential equations 3-8. For a given increment in time, Δt, the increment in inelastic strain and density are given by (for clarity, we temporarily drop the indicial notation on the strains/strain-rates, etc., and instead use a direct bolded notation, recognizing that the following apply for all of the components):

$$\Delta\boldsymbol{\varepsilon}^{in.} = (1-\beta)\dot{\boldsymbol{\varepsilon}}_t^{in.}\Delta t + \beta\dot{\boldsymbol{\varepsilon}}_{t+\Delta t}^{in.}\Delta t$$

$$\Delta\rho = (1-\beta)\dot{\rho}_t\Delta t + \beta\dot{\rho}_{t+\Delta t}\Delta t$$ Eq. 9

where the new subscripts denote the various quantities at times t and $t+\Delta t$. The value of $\beta = 0$ corresponds to a fully explicit scheme, whereas $\beta = 1$ corresponds to a fully implicit scheme. The derivatives at time t are expanded using Taylor series to give:

$$\dot{\boldsymbol{\varepsilon}}_{t+\Delta t}^{in.} = \dot{\boldsymbol{\varepsilon}}_t^{in.} + \frac{\partial\dot{\boldsymbol{\varepsilon}}^{in.}}{\partial\boldsymbol{\sigma}}\Delta\boldsymbol{\sigma} + \frac{\partial\dot{\boldsymbol{\varepsilon}}^{in.}}{\partial\rho}\Delta\rho + \frac{\partial\dot{\boldsymbol{\varepsilon}}^{in.}}{\partial T}\Delta T + O(h^2)$$

$$\dot{\rho}_{t+\Delta t} = \dot{\rho}_t + \frac{\partial\dot{\rho}}{\partial\boldsymbol{\sigma}}\Delta\boldsymbol{\sigma} + \frac{\partial\dot{\rho}}{\partial\rho}\Delta\rho + \frac{\partial\dot{\rho}}{\partial T}\Delta T + O(h^2)$$ Eq. 10

and Equation 5 can be written in incremental form as:

$$\Delta\boldsymbol{\sigma} = \underline{\underline{\mathbf{C}}}(\Delta\boldsymbol{\varepsilon}^{tot.} - \Delta\boldsymbol{\varepsilon}^{in.}) .$$ Eq. 11

Manipulation of Equations 9-11 resulted in a system of equations (7x7), with the six increments of stress and the increment of relative density as the unknowns. The system of equations was solved symbolically, using Mathematica, for those increments of

stress and the increment of relative density. The increments computed with Mathematica were then programmed directly into and used within the JAS3D constitutive model routine to advance the solution in time. In JAS3D, the stresses from the last converged solution are known. Estimates for the total strain rates are made for the next solution step based on the iterative solution algorithm. These strain rates are assumed to be constant over the solution step of interest. The stresses over the step are then computed in the constitutive routine using the equations presented above.

During the implementation of the SOVS constitutive model, care was taken to ensure that the implementation was consistent with and had the hooks necessary for integration with the 2D/3D mesoscale model sintering work of Tikare and Braginsky. This is important because it is anticipated that the mesoscale work will lead to significant improvements in our understanding of the sintering process at that scale which will result in a refinement of our capability to model at the continuum level. The capability to add this refinement as the mesoscale work progresses was of paramount importance.

2.0 Verification

The incremental implementation of the SOVS model in JAS3D has been verified by comparing the JAS3D solution to the following cases for which "analytic" solutions are available:

A uniaxial bar – sintering only;

A uniaxial bar – sinter forging case (1 MPa applied axial stress);

And a sphere – sintering only.

In all three cases the properties used were those for a 0.2 micron zinc oxide powder as reported by Olevsky, et. al (2001), namely: $P_{L_0} = 3\alpha / r_0$, with $\alpha = 1.27 \, \text{J/m}^2$ & $r_0 = 1 \, \square\text{m}$; and $\eta_0 = \left[51.7(T/750)^2 - 106.6(T/750) + 56.4\right] \times 10^{10} \, \text{Pa-s}$, with $750 \le T \le 1000 \, °\text{C}$ at 5°C/min. The initial porosity and the elastic properties used were: $\theta_0 = 53\%$; $E = 123.7 \times 10^9 \, \text{Pa}$; and $\nu = 0.356$.
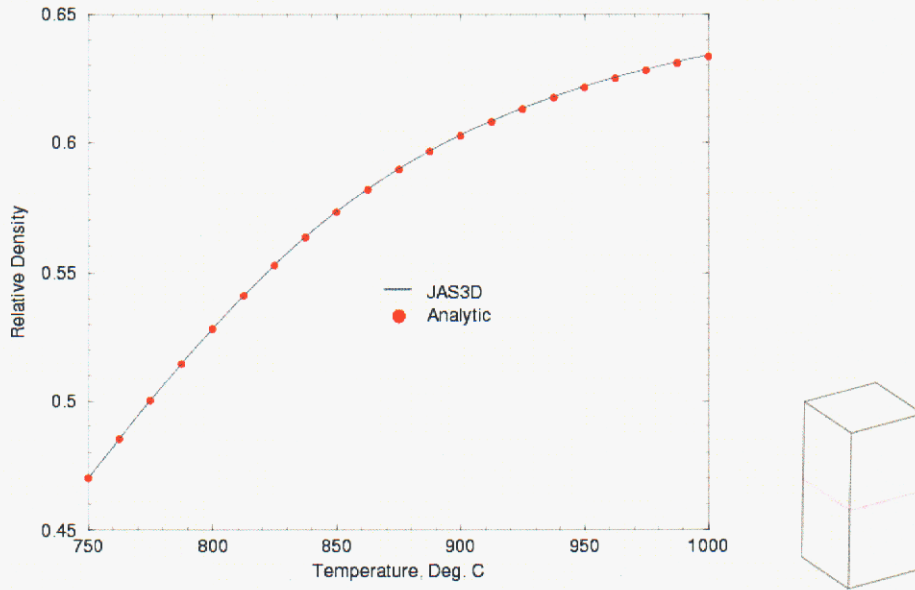
Figure 8. Uniaxial Bar Sinter-Only Verification Problem

2.1 Uniaxial Bar – Sinter-Only

The comparison of JAS3D to the analytic solution for the first case of a uniaxial bar subjected to sintering-only is shown in Figure 1. Also shown is the JAS3D mesh used
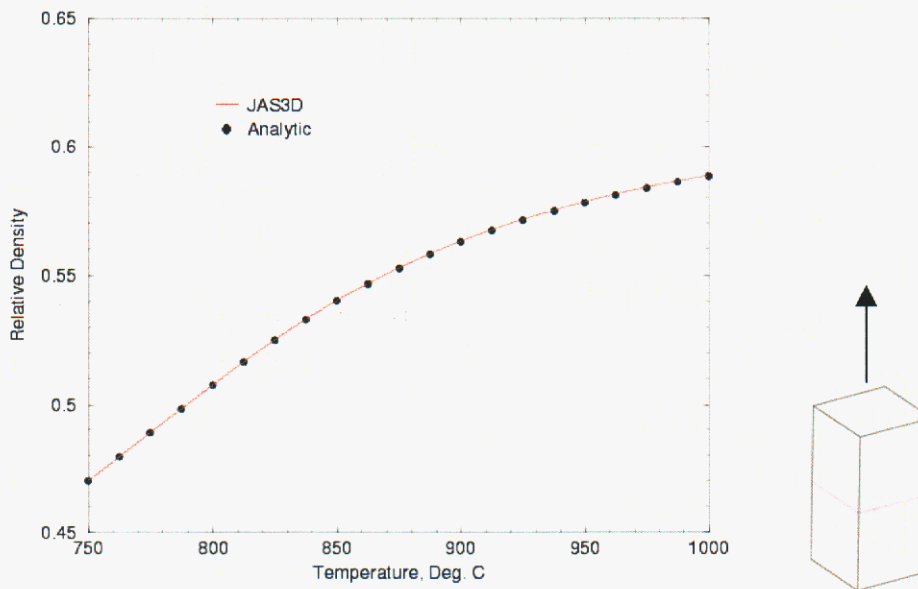
Figure 9. Uniaxial Bar Sinter-Forge Verification Problem

in the computation. This model contained two elements and 12 nodes, representing an octant of the overall model due to symmetry. In the process of verifying the implementation, we have started with the simplest case and slowly added complexity, so

this two-element model was an appropriate start. The JAS3D solution for the relative density essentially tracks the analytic solution.

2.2 Uniaxial Bar – Sinter-Forge

The results of a similar comparison for the same uniaxial bar but now with the added complexity of an additional 1 MPa applied axial tensile stress is shown in Figure 2. The tensile stress reduces the shrinkage in the axial direction such that the effective relative density of the body is reduced from the sinter-only case. Once again, the JAS3D solution for the relative density tracks the analytic solution.

2.3 Sphere – Sinter-Only

The comparison of JAS3D to the analytic solution for the third case of a sphere subjected to sintering-only is shown in Figure 3. Note that, again, only an octant of the sphere needed to be modeled with JAS3D because of symmetry. This particular model contained 304 elements and 420 nodes. The additional complexity in this case is the much larger model and the truly 3D effect of the modeled volume. Again, the JAS3D solution for the relative density tracks the analytic solution. In this case, the JAS3D solution shows the relative density calculated at the central element and at the elements at the three vertices of the model. The solutions for all of the elements overlay each other, as well as overlaying the analytic solution.
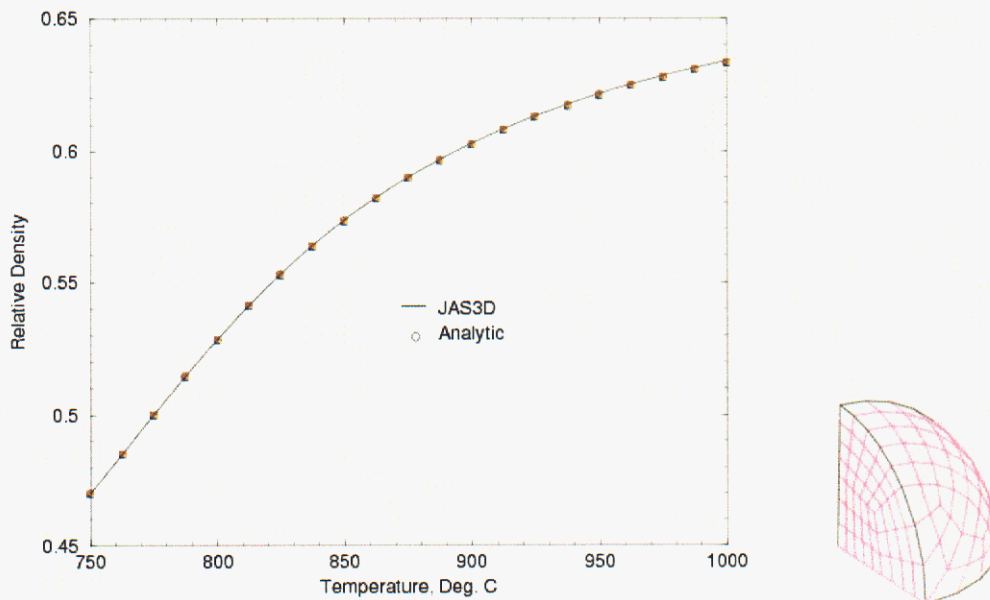

Figure 10. Sphere Sinter-Only Verification Problem

## 2.4 Numerical Performance of FEM Implementation

Convergence for the solution of general sintering-only problems with an iterative code such as JAS3D is a challenge. Typically convergence is measured by the relative imbalance of the internal forces to the applied loads. In a pure sintering simulation, there are no applied loads, so there is a need to devise a measure for determining when convergence is reached for this type of general problem. In all of the verification problems above, the solution was converged to very tight convergence tolerance to ensure accuracy. For larger production problems, such a tight convergence tolerance will probably be too costly, hence the need to address the issue. A scheme to converge this type of problems has been developed whereby an estimate of the sintering forces that act on the body is first made and then point one percent of that force is used as the allowable imbalance in the problem for convergence. Using this scheme, the performance of the model was investigated using a model problem similar to Garino's zinc oxide bi-layer bar experiment. This problem was assumed to be more representative in size of a production problem that the model would be used for. The computational performance of the model was investigated by varying the refinement (discretization) of the bi-layer bar and looking at its response as the refinement was increased from relatively coarse to very fine (hundreds of elements to tens-of-thousands of elements). It was found that the bulk response of the bar did not vary significantly with refinement and thus the bulk geometry of a part could be predicted without resorting to a very refined model. However, the details of the deformation were not adequately captured without significantly fine refinement. By this we mean that the curvature (and presumably warpage, etc.) that might be of interest to predict cannot be captured with this model unless a significant level of refinement is achieved. Problems in which accurate predictions of the details of the deformation of the part are sought will be computational expensive (requiring either long computations or the use of massively parallel computing).

3.0 Validation With Experiments

Having verified the incremental implementation of the SOVS constitutive in JAS3D and investigated and quantified its computational performance, the next step in the process was the validation of the model against a set of experiments. To this end, some of the sintering experiments of T. J. Garino on zinc oxide powder have been modeled using the SOVS model and comparisons with two of them are discussed below. In all cases, the same material properties as reported for the verification problems above were also used for the simulations of these experiments.

3.1 Bi-Layer Bar Experiment

The first of two experiments that we show comparisons for in this paper looked at the sintering of a bi-layer bar consisting of the same powder but at different starting relative densities of 47% for the upper layer and 57% for the lower layer. The bar was originally 8.049 mm long by 4.79 mm wide. The upper layer was 1.323 mm thick while the lower layer was 1.308 mm thick. Because the upper layer was at a lower starting density than the lower layer, it was expected that the final shape of the bar would be such that the overall bar would curve up as shown in the photograph of Figure 4. Using what we found from the computational performance study mentioned above, we used a very
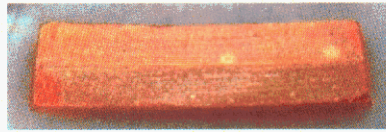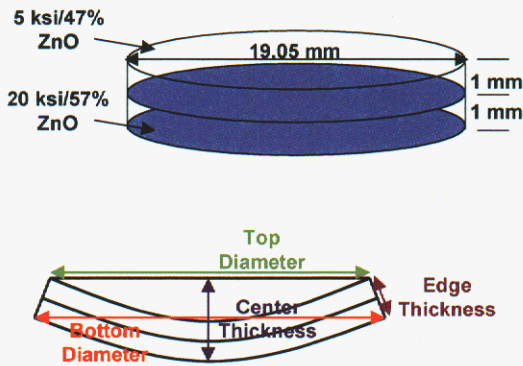
Experiment at 1001 °C

Simulation at 1000 °C

Sintering of ZnO (0.2µm) Bilayer Bar
Garino's Experiment vs. Simulation
$(\rho_{0u} = 0.47 \ \& \ \rho_{0l} = 0.57)$

	Experiment	Simulation	Difference
L (8.049 mm)	6.7	6.431	4.0%
H_u (1.323 mm)		1.001	

fine mesh to model this experiment (138,000 elements for a quarter model). The results from the JAS3D simulation was then compared to the data obtained from the experiment. Figure 4 shows a comparison of the predictions to the experiment. Both qualitative and quantitative comparisons were made. The simulation and the experimental results show very good agreement both in the bulk response as well as in the details (i.e., the curvature).

3.2 Bi-Layer Disk Experiment

A second experiment, for which comparisons with the model are included in this paper, was a bi-layer disk experiment performed by Garino using the same ZnO powder but at different starting relative densities of 47% for the upper layer and 57% for the lower layer. So once again, the disk was expected to curve up similar to the shape shown schematically in Figure 5. The disk was originally 19.05 mm in diameter and each layer was 1 mm thick. The schematic of the experiment and the measured quantities along with a qualitative comparison of the experiment to the simulation are shown in Figure 5. Once again, we see relatively good agreement between the measured and computed results. The bulk computed responses of the disk are within 2% of the measured bulk responses. The computed "center thickness," which is an indirect measure of the warpage of the disk, differs from the measured value by only 13.7%.

5 ksi/47% ZnO

19.05 mm

1 mm
1 mm

20 ksi/57% ZnO

Top Diameter

Center Thickness

Edge Thickness

Bottom Diameter

Sintering of ZnO (0.2µm) Bilayer Disk Garino's Experiment vs. Simulation
($\rho_{0u} = 0.47$ & $\rho_{0l} = 0.57$)

At 925 °C	Experiment	Simulation	Difference
D_T (19.05 mm)	15.24	15.04	1.3%
D_B (19.05 mm)	15.66	15.98	2.0%
T_E (2.00 mm)	1.63	1.61	1.1%
T_C (2.00 mm)	2.72	2.35	13.7%

Figure 12. Comparison of Simulation to Garino's Bi-Layer Disk Experiment

4.0 Summary & Conclusions

A continuum capability for modeling linear-viscous sintering has been developed, implemented, and demonstrated. The implementation uses the Skorohod-Olevsky viscous sintering constitutive description. The overall capability is based on a finite element formulation that allows 3D components to be modeled using SNL's nonlinear large-deformation finite element code, JAS3D. This computational tool provides us with the ability to model sintering of complex three-dimensional components. The implementation has been verified against simple problems with known solutions. The numerical performance of the implementation has been explored and quantified. The capability has been validated with laboratory-scale experiments, performed by Garino, on ZnO powder. The implementation has the necessary interfacing to couple with the results from the sintering meso-scale modeling research being conducted by Tikare and Braginsky. The model can mimic measured relative densities and measured bulk and detailed deformations in the laboratory-scale experiments to within a few percent, indicating that the model is capable of capturing linear-viscous sintering behavior in ZnO.

References

1. McHugh, P. E. and H. Riedel, "A Liquid Phase Sintering Model: Application to Si_3N_4 and WC-Co," *Acta Mater*. Vol. 45, pp. 2995-3003, 1997.
2. Olevsky, E. A., "Theory of Sintering: From Discrete to Continuum," *Materials Science and Engineering*, R23, pp. 41-100, 1998.
3. Olevsky, E. A., V. Tikare, T. J. Garino, and M. V. Braginsky, "Simulation of Sintering of Layered Structures," *Proceedings of the World Congress on Powder Metallurgy, November 1999*, Kyoto, Japan, 2000.
4. Skorohod, V. V., *Rheological Basis of the Theory of Sintering*, Naukova Dumka, Kiev, 1972.
5. Tikare, V. and M. V. Braginsky, "Modeling Microstructural Evolution During Sintering in a Complex Powder Compact, Proceedings of MRS 2002,

Chapter 6
Numerical Simulation of Anisotropic Shrinkage in a 2D Compact of Elongated Particles

Veena Tikare, Michael Braginsky, Eugene Olevsky and D. Lynn Johnson

Abstract

Microstructural evolution during sintering of 2D compacts of elongated particles packed in different arrangements was simulated using a kinetic, Monte Carlo model. The model used simulates curvature driven grain growth, pore migration, vacancy formation and annihilation. Only the shape of the particles was anisotropic; all other extensive thermodynamic and kinetic properties such as surface energies and diffusivities were isotropic. We verified our model by simulating sintering in the analytically tractable case of simple-packed, elongated particles and comparing the shrinkage rates to those predicted analytically. Once our model was verified, we used it to simulate sintering in different geometries of elongated particles to gain understanding of differential shrinkage.

Anisotropic shrinkage occurred in all compacts with aligned, elongated particles. However, the direction of higher shrinkage was in some cases along the direction of elongation and in other cases in the perpendicular direction depending on the details of the powder compact. In compacts of simple-packed, mono-sized, elongated particles, shrinkage was higher in the direction of elongation. In compacts of close-packed, mono-sized, elongated particles and of elongated particles with a size and shape distribution, the shrinkage was lower in the direction of elongation. The results of these simulations are analyzed and the implication of these results is discussed.

1.0 Introduction

An inescapable reality of ceramic processing is that almost all ceramics shrink at least 30% and as much as 50% in volume during sintering. This enormous dimensional change causes distortions in the shape and, in the extreme, fracture of the ceramic during sintering. The ability to predict and control these shape distortions has to a large extent determined the shape and size of ceramic products that could be manufactured. The tolerances to which dimensional changes need to be controlled continue to become increasingly tighter and limit the advance of many new technologies. One example is wireless communication technology, which relies on highly integrated, miniaturized components imbedded in multilayered ceramics (MLCs). Dimensional control due to sintering of the multimaterial components and circuitry is critical for optimal performance of such systems.

In addition to the obvious difficulties of co-sintering different materials with different shrinkage rates, more subtle effects lead to warpage during sintering of tape cast ceramic layers used in MLCs. The individual ceramic layers themselves have some shrinkage anisotropy upon sintering. Raj and Cannon[1] have reviewed a number of experimental works[2,3,4,5,6,7,8,9,10,11,12,13,14,15,16] that show anisotropic shrinkage primarily in

tape cast ceramics. Most attributed the anisotropic shrinkage to the alignment of non-equiaxed particles and some to differential spacing of particles during green processing due to differential aging[5,6] or relaxation[7] of the binders. In their own work, Raj and Cannon show that shrinkage results from particle orientation by the tape cast process. In all these works, the anisotropic shrinkage originated from inhomogeneities in green processing rather than from anisotropic thermodynamic or kinetic quantities. Raj et al.[17] also simulated shrinkage in a system of perfectly packed elliptical particles using numerical methods developed by Zhang and Schneibel[18]. They reported that shrinkage rates in the transverse direction (direction perpendicular to elongation) decreased as sintering progressed, particularly when grain boundary diffusion was much lower than surface diffusion.

In this work, we seek to understand the origin of anisotropic shrinkage by simulating sintering in systems that have aligned, elongated particles with isotropic thermodynamic properties, such as surface energy, and isotropic kinetic properties, such as diffusitivity. We simulate shrinkage during sintering in several highly aligned system of mono-sized and distributed-sized, elongated particles. The motivation is to explore and understand the mesoscale behavior by examining the microstructural evolution of elongated particles and the pore geometries. We also studied the shrinkage of powder compacts in the directions parallel and perpendicular to elongation and attempted to understand how microstructural evolution influenced shrinkage.

2.0 Model and Simulation Method

The two-dimensional model presented here is limited to consideration of the following processes:

Grain growth by short range diffusion of atoms from one side of the grain boundary to the other;
Long range diffusion of material to pores by grain boundary diffusion and along pore surfaces by surface diffusion;
Vacancy annihilation at grain boundaries.

This model has been presented in a previous work and shown to simulate all these processes correctly[19]. In the model, an ensemble of grain sites and pore sites is allowed to populate a square lattice. The grain site can assume one of many degenerate states, $q_{grain} = [1, 2 ...Q]$ where Q is the total number of grain states and q is the state of a grain site. The pore sites can assume only one state, $q_{pore} = -1$. Contiguous grain sites of the same state q form a grain and contiguous pore sites form a pore. Grain boundaries exist between neighboring grain sites of different states, q, and pore-grain interfaces exist between neighboring pore and grain sites. The equation of state for these simulations is the sum of all the neighbor interaction energies in the system given by

$$E = \frac{1}{2}\sum_{i=1}^{N}\sum_{j=1}^{8}\left(1 - \delta\left(q_i, q_j\right)\right) \qquad \text{eq. 1}$$

where N is the total number of sites, δ is the Kronecker delta with $\delta(q_i = q_j) = 1$ and $\delta(q_i \neq q_j) = 0$, q_i is the state of the grain or pore at site i and q_j is the state of the nearest neighbor at site j. Thus, the only energy considered in the simulation is the interfacial energy and all unlike neighbors contribute one arbitrary unit of energy to the system. As pore sites can assume only one state, $q_{pore} = -1$, there are no pore boundaries and all pore sites coalesce. In contrast, grain sites can assume many states making grain boundaries possible. This yields a two-component, two-phase system with uniform, isotropic interfacial energies between grains and between grains and pores.

Grain growth is simulated using the method developed in previous works[20,21]. First, a grain site is chosen at random from the simulation space. Then, a new state q_{grain} is chosen at random from all neighboring grain states. The grain site is temporarily assigned the new state and the change in energy is evaluated using equation 1. Next, the standard Metropolis algorithm[22] is used to perform the grain growth step based on Boltzmann statistics. A random number, R, between 0 and 1 is generated. The transition probability, P, is calculated using

$$P = \begin{cases} \exp\left(\dfrac{-\Delta E}{k_B T}\right) & \textit{for} \quad \Delta E > 0 \\[2em] 1 & \textit{for} \quad \Delta E \leq 0 \end{cases} \qquad \text{eq. 2}$$

where k_B is the Boltzmann constant and T is the simulation temperature, a variable that defines the degree of thermal fluctuation in the system. If $R \leq P$, then the grain growth step is accepted, if not, the original state is restored. The simulation temperature used for grain growth was $k_B T = 0$, which has been shown to simulate grain growth correctly[21]. Note that at $k_B T = 0$, all grain growth steps that result in higher energy are not accepted, only equal energy or lower energy grain growth steps are accepted.

Pore migration is simulated using conserved dynamics, so that the total number of pore sites and grain sites is the same after a pore migration step. A pore site is chosen and a neighboring site is chosen at random. If the neighboring site is a grain site, the two sites are temporarily exchanged with the grain site assuming a new state q_{grain}, where q_{grain} results in the minimum energy. This minimum-energy, pore-grain exchange simulates pore migration by surface diffusion[23]. The change in energy for this exchange is calculated using equation 1 and again the standard Metropolis algorithm is used to perform the pore migration step using equation 2 to determine the transition probability. The simulation temperature used for the pore migration step was $k_B T = 0.7$. This higher temperature was necessary to simulate pore migration and is discussed in other works[23].

Densification in crystalline solids occurs by uniform annihilation of vacancies at the grain boundaries[24,25,26]. As vacancies are annihilated, the center of mass of the adjoining grain moves toward the grain boundary, thus giving densification. The rate-limiting step in this process is for the vacancies to diffuse along a distance proportional to

the length of the grain boundary. In this model a vacancy is defined as a single, isolated pore site that is not connected to any other pore sites. The algorithm used for vacancy annihilation is the following. A pore site is chosen. If it happens to be a vacancy (an isolated pore site) on a grain boundary, it is annihilated.

Annihilation is simulated as follows. A straight line is drawn from the isolated pore site through the center of mass of the adjacent grain to the simulation boundary. Next, the isolated pore site and the boundary grain site are exchanged with the grain site assuming the q state of the adjacent grain. This algorithm conserves mass globally, moves the center of mass of the adjacent grain towards the annihilation site, and annihilates a vacancy. The frequency of the annihilation attempts is adjusted to simulate the diffusion of vacancies along the grain boundary. As the grain boundary length increases, time between annihilations also increases as:

$$ t_{anni} = t_{anni}^{i} \left(\frac{L_{gb}}{L_{gb}^{i}} \right)^{2} \qquad \text{eq. 3} $$

where t_{anni} is the time between annihilation attempts, t_{anni}^{i} is the time between annihilation attempts for the initial grain boundary length L_{gb}^{i} at the beginning of sintering, and L_{gb} is the current grain boundary length. Adjusting the annihilation frequency in this manner simulates uniform annihilation of vacancies along the grain boundary.

Sintering is simulated by attempting the grain growth, pore migration and vacancy annihilation steps in sequence, repeatedly. Time in the model is measured in units of Monte Carlo step; 1MCS corresponds to N attempted changes where N is the total number of sites in the system. MC time is linearly proportional to real time[27] in material systems that have the characteristics simulated by the model. The proportionality constant of a given material can be found by comparing simulated microstructural evolution to that of the material. Three different geometries were simulated, (1) simple-packed, mono-sized elongated particles as shown in figure 1, (2) close-packed, mono-sized elongated particles shown in figure 5, and (3) elongated particles with a wide size distribution packed so that their long axis is aligned primarily in one direction as shown in figure 8a. The grain growth, pore migration and annihilation algorithms are applied as described above to simulate sintering. Shrinkages in the X- and Y-directions are measured as functions of time.

3.0 Analytical Solution

To verify our simulation results, an analytic solution for shrinkage was determined. Following the analysis of Johnson[25], the shrinkage anisotropy was predicted for the geometry shown in figure 1. Johnson calculated shrinkage rate by equating the
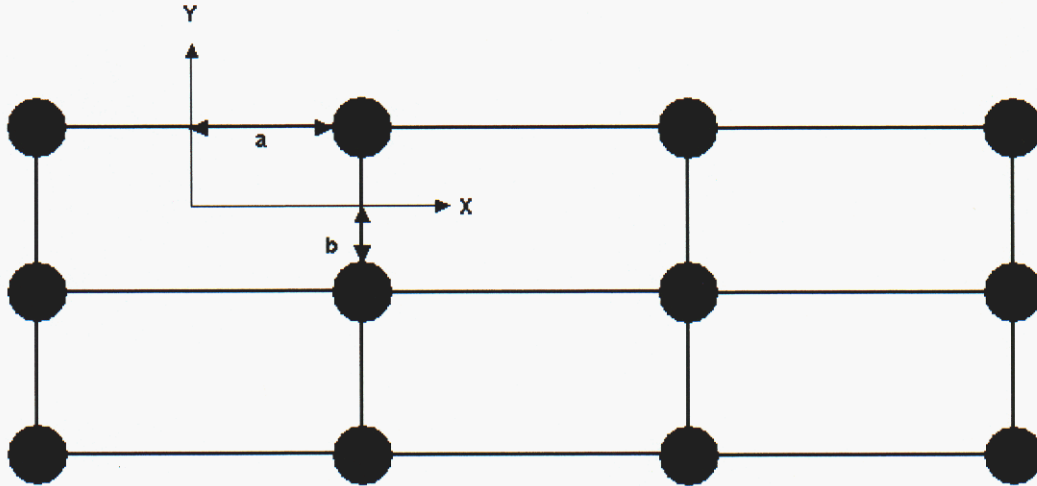

Figure 1. Schematic showing the initial microstructure used to calculate shrinkages in the X- and Y-directions analytically.

flux of material to the pore to the change in pore size due to the material flowing in. The flux was due to the chemical potential gradient along the grain boundaries due to the stress applied normal to the grain boundaries by the pores. The only transport mechanism considered is grain boundary diffusion. The fluxes along the two sets of grain boundaries in the X- and Y-directions, respectively, are

$$J_x = -\frac{D\delta}{\Omega kT}\frac{d\mu}{dx} \quad \text{and} \quad J_y = -\frac{D\delta}{\Omega kT}\frac{d\mu}{dy} \qquad \text{eq. 4}$$

where J_x and J_y are the fluxes along the X-orientated and Y-orientation grain boundaries, D is grain boundary diffusivity, δ is grain boundary thickness, Ω is molar volume, k is Boltzmann's constant, T is temperature, and μ is chemical potential.

Since all transport except grain boundary diffusion is negligible, continuity requires that

$$\nabla J = const \qquad \text{eq. 5}$$

Furthermore, the chemical potential μ and stress normal to the grain boundary σ are related as

$$\nabla \sigma = \frac{\nabla \mu}{\Omega} \qquad \text{eq. 6}$$

The solution to the stress (or chemical potential) equation is of the form

$$\sigma = c_{1i}x^2 + c_{2i}x + c_{3i} \qquad \text{eq. 7}$$

where i denotes either the X- or Y-direction, c_{1i}, c_{2i} and c_{3i} are constants. Two boundary conditions can be deduced. By symmetry, stress gradient at the center of the neck, $x = 0$ and $y = 0$, is $\nabla \sigma_i = \mathbf{0}$, which gives $c_{2i} = 0$. Stress at the pore surface, $x = a$ and $y = b$, is given by the Gibbs-Thompson relation $\sigma_i = -\dfrac{\gamma}{r}$ where γ is the surface energy and r is the pore radius of curvature, which gives $c_{3x} = -c_{1x}a^2 - \dfrac{\gamma}{r}$ and $c_{3y} = -c_{1y}b^2 - \dfrac{\gamma}{r}$.

Finally, the force balance on the grain boundary requires

$$\int_0^a \sigma\, dx = \gamma \sin\frac{\theta}{2} \qquad \text{and} \qquad \int_0^b \sigma\, dy = \gamma \sin\frac{\theta}{2} \qquad \text{eq. 8}$$

where θ is the dihedral angle. Substituting equation 7 into 8 and solving for c_{1i} gives

$$c_{1x} = -\frac{3\gamma\left(r\sin\dfrac{\theta}{2} + a\right)}{2a^3 r} \qquad \text{and} \qquad c_{1y} = -\frac{3\gamma\left(r\sin\dfrac{\theta}{2} + b\right)}{2b^3 r}.$$

Substituting these into equation 7 and using equation 4 gives the fluxes into the pore along the X- and Y-oriented grain boundaries from 0 to a and 0 to b, respectively

$$J_x = \frac{3\delta D\gamma}{kTa^2 r}\left(r\sin\frac{\theta}{2} + a\right) \qquad \text{eq. 9a}$$

and

$$J_y = \frac{3\delta D\gamma}{kTb^2 r}\left(r\sin\frac{\theta}{2} + b\right) \qquad \text{eq. 9b}$$

If we consider a unit cell with a pore at the center, with original height $2(b_o + r_o)$ and length $2(a_o + r_o)$, we can see that a total flux of $2J_x dt$ comes in during time element dt. This causes a collapse of an amount $d\Delta_y$, giving mass of $2ad\Delta_y$ flowing into the pore. Thus

$$J_x \Omega dt = ad\Delta_y \qquad \text{and} \qquad J_y \Omega dt = bd\Delta_x \qquad \text{eq. 10}$$

where Δ_x and Δ_y are the change in grain length in the X- and Y-directions, respectively. Shrinkage rate is defined as

$$s_x = \frac{d}{dt}\left(\frac{\Delta_x}{2(a_o + r_o)}\right) \qquad \text{and} \qquad s_y = \frac{d}{dt}\left(\frac{\Delta_y}{2(b_o + r_o)}\right) \qquad \text{eq. 11}$$

where a_o, b_o and r_o are the initial dimensions. Substituting equations 10 into 11 and taking the ratio of the two shrinkage rates

$$\frac{s_x}{s_y} = \left(\frac{b_o + r_o}{a_o + r_o}\right)\left(\frac{r\sin\dfrac{\theta}{2} + b}{r\sin\dfrac{\theta}{2} + a}\right)\frac{a^3}{b^3}$$ <div align="right">eq. 12</div>

Thus, we find that the ratio of shrinkage rates is a function of the grain and pore dimensions for the geometry shown in figure 1.

Results

4.1 Model verification by comparison of simulation results to the analytical solution

The sintering simulations were run using the grain growth, pore migration and vacancy annihilation steps as described previously. The microstructural evolution of the system is shown in figure 2.
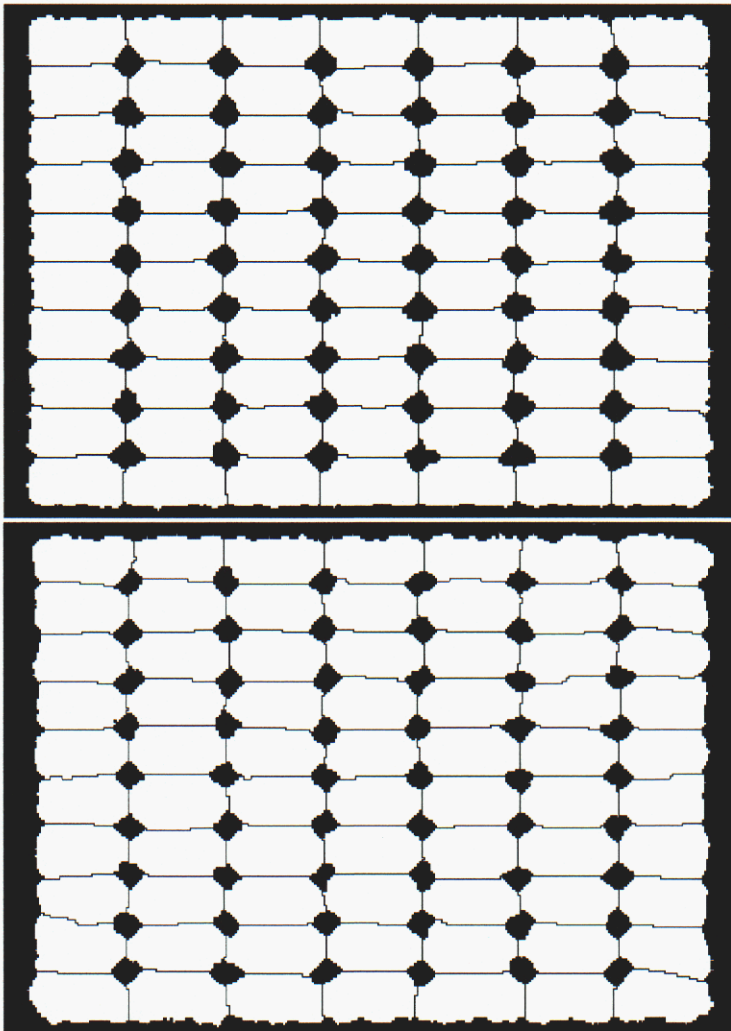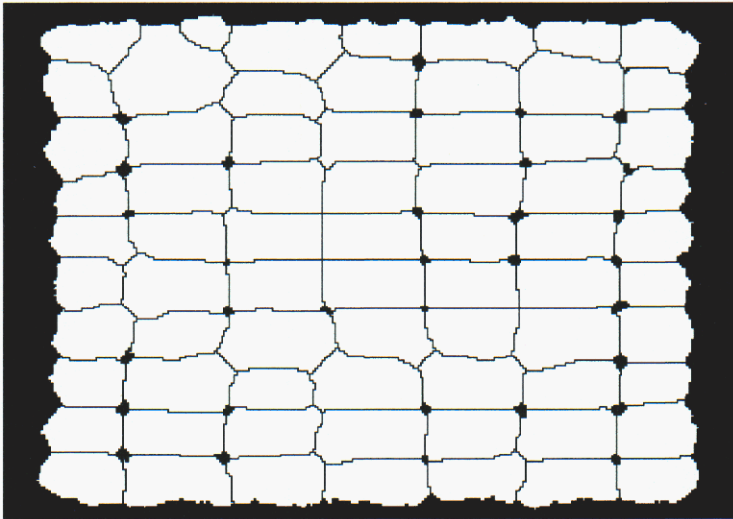
Figure 2. Microstructural evolution during sintering of simple-packed, elongated particles from the (a) initial microstructure, at (b) time = 50,000 MCS and, (c) time = 219,000 MCS.

The starting configuration is perfectly elongated particles with pores at all the grain junctions. As the simulation progresses, vacancies are formed at the pore surfaces and diffuse along grain boundaries. They are annihilated at the grain boundaries. This leads to densification of the system. Grain growth does not occur while the pores are present at the junctions and none is expected, as the grain boundaries are not curved. However, once the pores shrink away and four grains meet to form a quadra-junction, they quickly grow in a manner so as to eliminate the quadra-junction and form a triple junction as seen in figure 2c. Again this is expected as quadra-junctions are unstable configurations in a system with uniform grain boundary energies. While the shapes of pores do fluctuate around the minimum energy shape, they do not migrate as they cannot detach from the grain boundaries. The simulations show greater shrinkage in the direction of elongation (X-direction) than perpendicular to elongation (in the Y-direction).

The shrinkages in the X- and Y-directions measured during the sintering simulations are plotted in figure 3 as functions of time for the case shown in figure 2. As the microstructures in figure 2 suggested, shrinkage in the direction of elongation is larger than that perpendicular to it. The grain boundary lengths, a and b, and the pore size r were measured for the simulation shown in figure 2 and used to calculate the predicted shrinkage rate ratio using equation 12. The shrinkage ratios measured from the simulation are in good agreement with the analytically predicted ratio as shown in figure 4 during sintering of elongated, simple-packed particles.
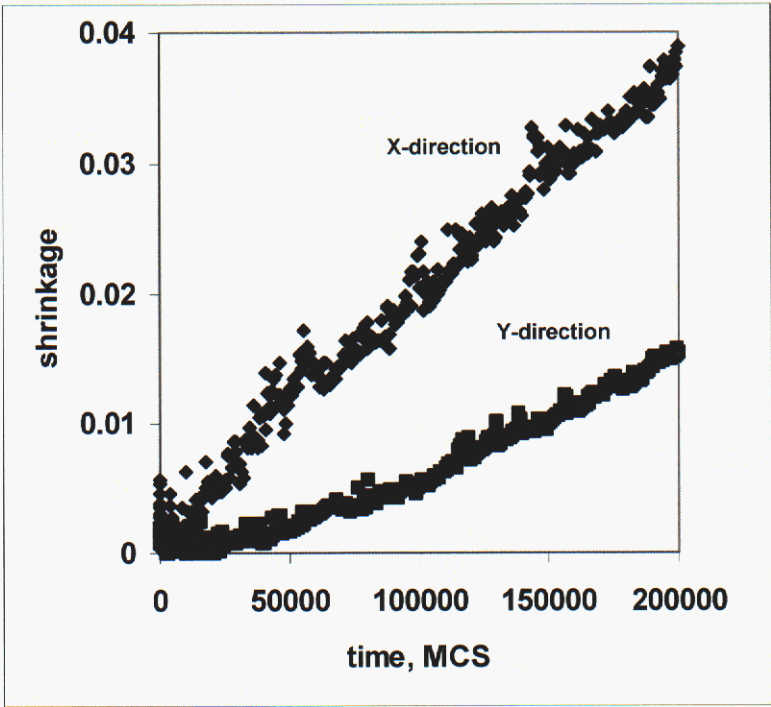
Figure 3. Shrinkage in the directions parallel (X) and perpendicular (Y) to elongation during sintering of simple-packed, elongated, monosized particles.
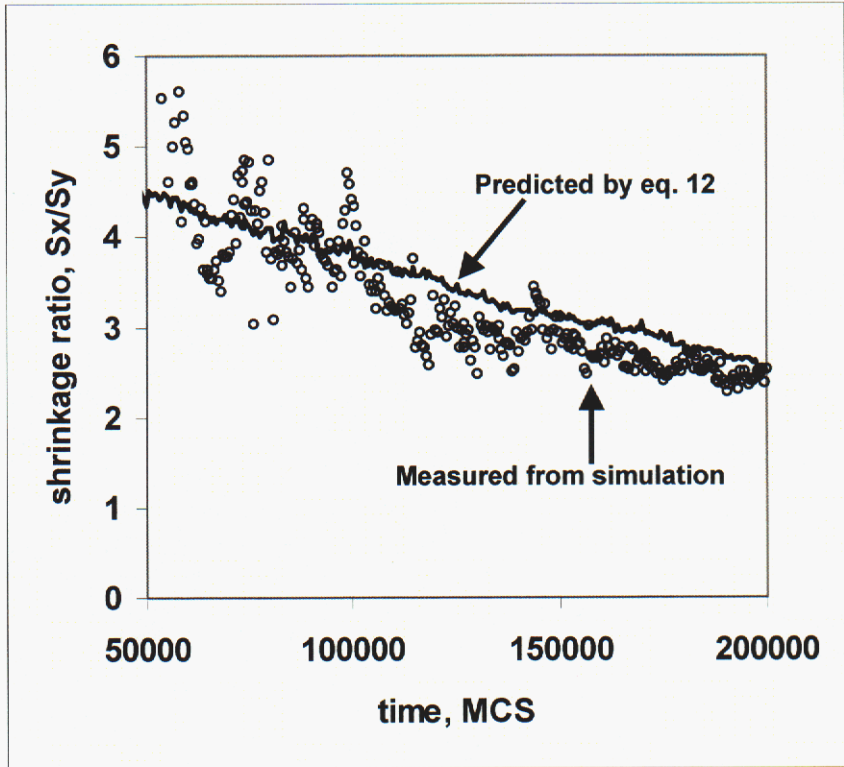

Figure 4. Comparison of shrinkage ratio measured from simulation to that predicted sintering theory given in eq. 12.

4.2 Simulation of sintering in other compacts of elongated particles

We used the verified model to simulate sintering in other compacts of elongated particles. The next geometry that was simulated was a 2D compact consisting of close-packed, elongated particles with pores at all the grain junctions, figure 5. The microstructure evolution of this system is shown in figure 6. As in the previous set of simulations, the vacancies are formed at the pore surface, diffuse along grain boundaries and are annihilated at a uniform rate at the grain boundaries. This leads to densification of the system. Grain growth does not occur while the pores are present at the junctions and none is expected, as the grain boundaries are not curved. However, once pores disappear at the junctions, grains are no longer pinned and rapidly grow until they are pinned by the next set of pores as seen in figure 6c. The shrinkage in this system is also anisotropic, however, it is in the opposite direction as shown by figure 7, a plot of shrinkages in the X- and Y-directions as functions of simulation time. Shrinkage perpendicular to the direction of elongation (the Y-direction) is higher. This predicted by the analytical model. Equations 9 and 10 and the first equation 11 still obtain, with *a* and *b* as defined in figure 5. However, the second equation 11 must be multiplied by 2, since there are now two grain boundaries in the Y-direction in the unit cell of the microstructure. Thus, the ratio of shrinkage rates for this geometry is

$$\frac{s_x}{s_y} = \frac{1}{2}\left(\frac{b_o + r_o}{a_o + r_o}\right)\left(\frac{r\sin\frac{\theta}{2} + b}{r\sin\frac{\theta}{2} + a}\right)\frac{a^3}{b^3} \qquad \text{eq. 13}$$
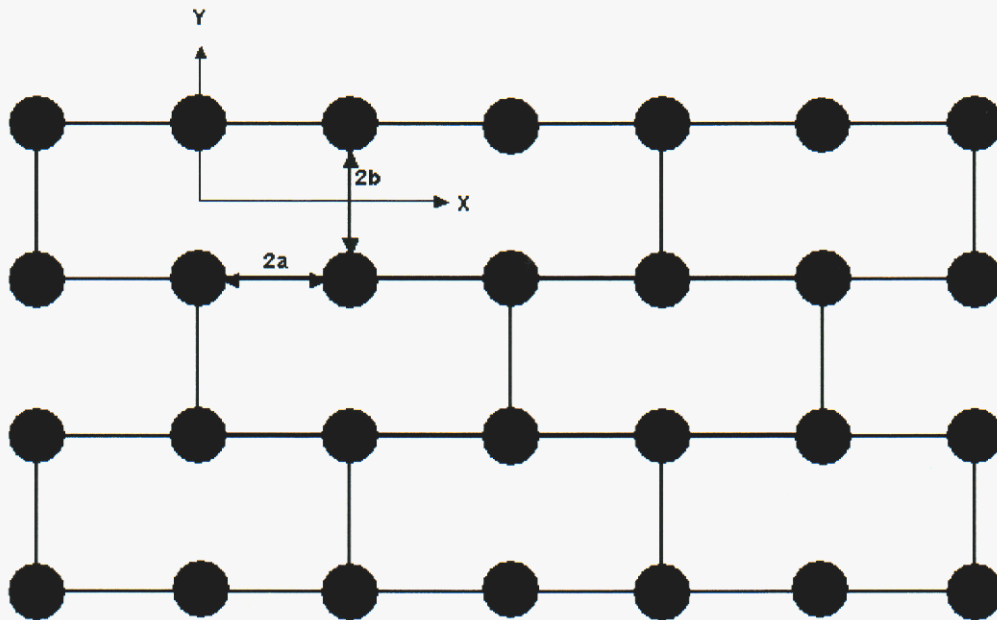

Figure 5. Schematic showing the initial arrangements of close-packed, elongated particles sintering.

Examination of the microstructure shows that for the geometry in figure 6, the concentration gradients along the grain boundaries in the X- and Y-directions are almost identical as the pore size and grain boundary length are similar in both directions ($a \approx b$). However, the grain boundary length per unit area in the X-directions is approximately double that in the Y-direction. Therefore, twice as many annihilations per unit area of simulation space occur at grain boundaries in the X-direction leading to higher shrinkage in the Y-direction as predicted by eq. 13. Note that if a was sufficiently larger than b, then the direction of higher shrinkage would be change from the Y-direction to the X-direction.
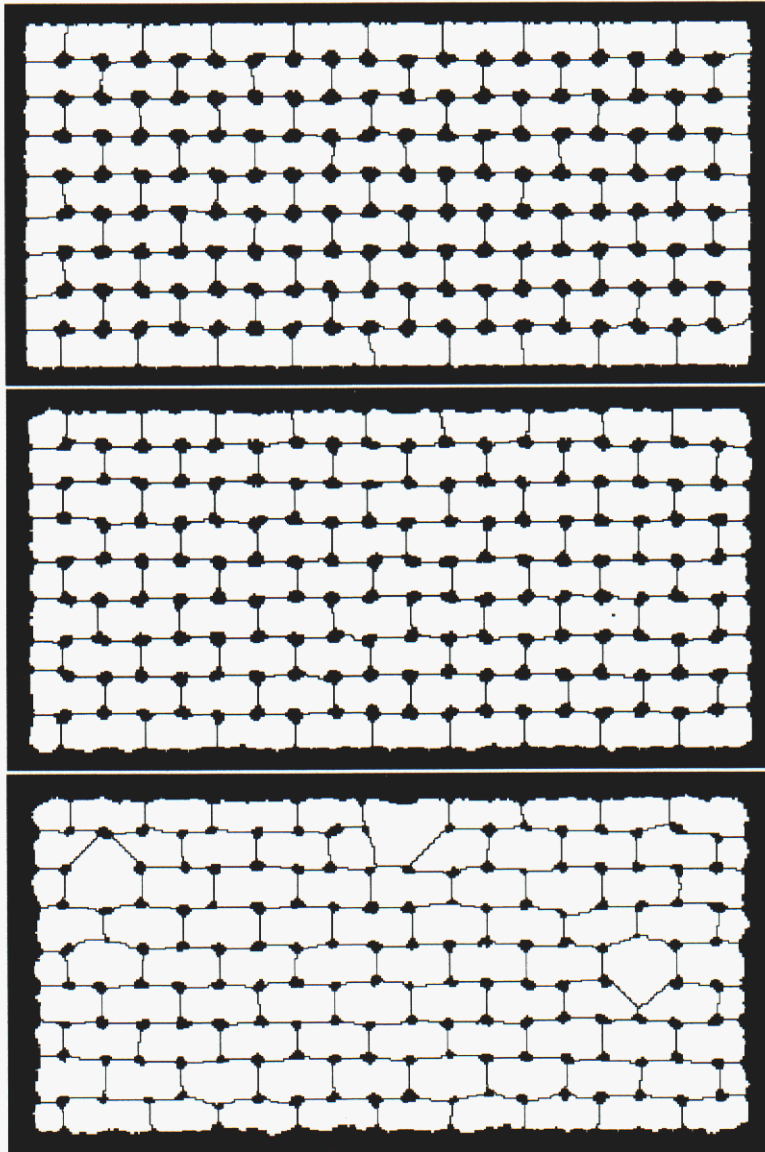

Figure 6. Microstructural evolution during sintering of closed packed elongated particles from the (a) initial microstructure, at (b) time = 9,000 MCS, and (c) time = 22,000 MCS.
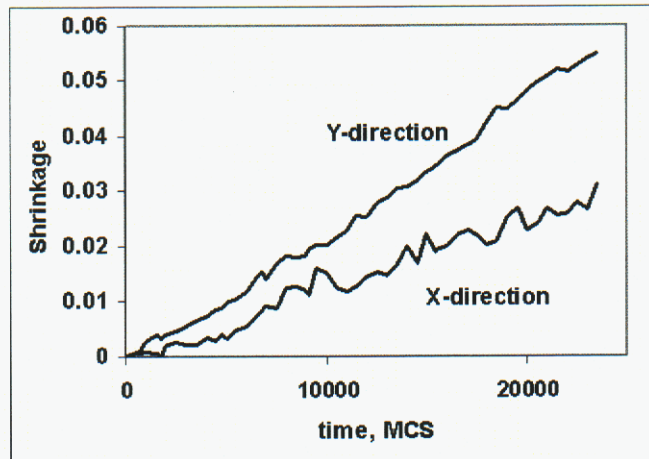
Figure 7. Shrinkage in the directions parallel (X) and perpendicular (Y) to elongation during sintering of close-packed, elongated particles.

The final microstructure that we studied was one with elongated particles of arbitrary sizes and shapes. We obtained the starting microstructure for this simulation by generating an equi-axed microstructure then stretching it in one direction, the X-direction, to double its former length. The starting microstructure is shown in figure 8a. Unlike the previous cases, the particles and pores are of different sizes and shapes. Furthermore, while particles are elongated in the X-direction, they are not perfectly aligned in this direction as in the previous simulations. The subsequent microstructural evolution is also shown in figure 8. Many differences were seen in this simulation from the previous cases. Initially, both grains and pores are elongated, however, pores became equi-axed very quickly by surface diffusion, whereas grains remained elongated much longer. Since grain boundaries have curvature, grains grew. Pores continue to pin grain growth, however, they move due to the curved grain boundaries exerting uneven force on them. As pores move, they coalesce to form larger pores. These pore coalescence events allow grains to grow locally. Pores grow by coalescence, but also shrink at the same time by vacancy formation and annihilation, which in turn leads to densification. Another important difference to note is that as the microstructure coarsened, grains grew increasingly more equi-axed.
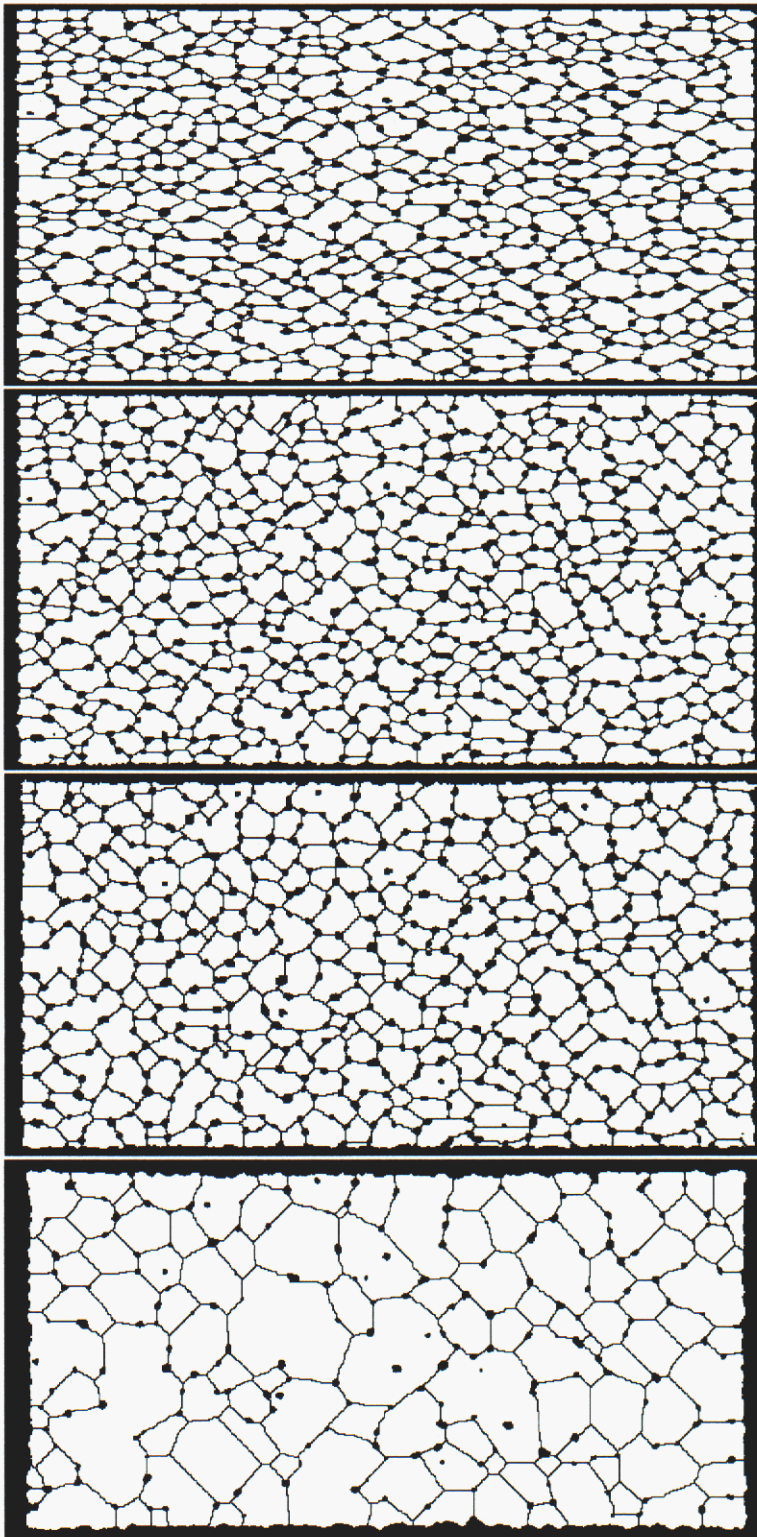
Figure 8. Microstructural evolution in randomly packed elongated particles of arbitrary size and shape for (a) the initial microstructure and at (b) time = 1,000 MCS, (c) time = 7,000 MCS and (c) time = 30,000 MCS.

Shrinkage during sintering in the directions parallel and perpendicular to elongation is shown in figure 9. The densification behavior of a powder compact with elongated particles of arbitrary sizes and shapes was also different from the cases of perfectly packed, mono-sized particles. The densification rate decreased as the grain grew. This is to be expected as the diffusion distance for vacancies along grain boundaries increased. In the perfectly packed simulations, grain growth was pinned and the distance for vacancies to diffuse remained virtually constant until pores disappeared, thus giving constant shrinkage rates. Anisotropic shrinkage was observed in this system too, with lower shrinkage in the direction of elongation. However, the anisotropy in shrinkage rates decreased with time as the microstructure became more isotropic.
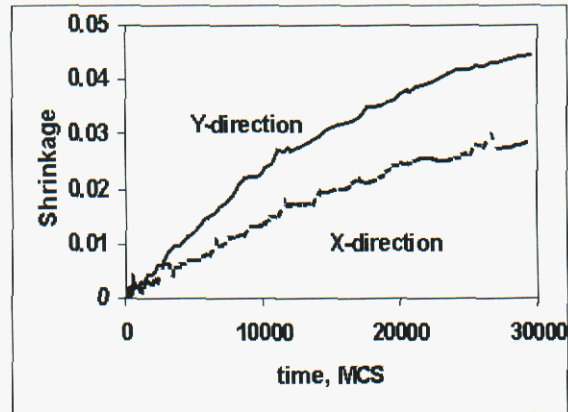

Figure 9. Shrinkage in the directions parallel (X) and perpendicular (Y) to elongation during sintering in powder compacts of particles of arbitrary shape and size.

5.0 Discussion

Simulations in the previous section have shown that anisotropic shrinkage can occur when elongated particles are compacted with particles aligned in one direction. However, highly anisotropic shrinkage can occur with higher shrinkage in the direction of elongation or in the perpendicular direction depending on the details of particle and pore arrangement. If particles and pores are arranged so that annihilations occur preferentially along grain boundaries oriented in certain directions, then shrinkage occurs preferentially in the direction perpendicular to that direction. In the first case studied and shown in figures 2 and 3, annihilations occurred primarily at grain boundaries aligned perpendicular to the direction of elongation. Thus, shrinkage occurred preferentially in the direction of elongation. In the next two cases studied and shown in figures 5 to 9, preferential shrinkage occurred perpendicular to the direction of elongation as more vacancies were annihilated at grain boundaries aligned in the direction of elongation. This apparently contradictory shrinkage behavior from microstructures that are very similar was unexpected. However, it is clear from the simulation that microstructures with similar characteristics can give differing anisotropic shrinkage behavior not just in magnitude, but also in the preferential shrinkage direction. These observations may explain why different experiments studying anisotropic shrinkages due to different tape casting processing methods have given what appear to be contradictory results.

In this work, we simulated systems with highly elongated, aligned particles that sintered with highly exaggerated shrinkage anisotropy to emphasize the cause of the shrinkage anisotropy. In real material systems such as MLCs, the shrinkage anisotropy is much less with differences in shrinkage ranging up to a few percent. This is due to a variety of reasons. The powders used for MLCs are made from nominally equi-axed particles; tape casting just aligns particles that deviate slightly. Thus, neither the particles nor the alignment due to the tape casting process is as exaggerated as the structures presented in figures 2, 6 and 8. However, in all cases, the origin of anisotropic shrinkage is the same; it is that annihilations occur preferentially along grain boundaries oriented predominately in one direction.

While there are limitations, the simulations in this paper demonstrate the utility of this sintering model. A limitation of this sintering model is that it is applicable to situations where uniform shrinkage occurs and thus, there are no long-range stresses due to differential sintering. The model also assumes that grain boundary sliding is facile so that shrinkage at the various grain boundaries is independent of each other. In spite of these limitations, the model is useful to understand sintering under many different conditions. Furthermore, this model makes very few assumptions about the geometry of grains and pores. Many different types of data can be mined from the microstructural evolution simulations. Shrinkage in any direction, grain and pore size, grain and pore shape, grain boundary and pore surface length and many other features can be measured during sintering and correlated with each other to gain an understanding of sintering.

6.0 Conclusions

A kinetic, Monte Carlo model was used to simulate microstructural evolution in two dimensional powder compacts of aligned, elongated particles with particular attention given to directional shrinkage in the direction of elongation and in the direction perpendicular to elongation. Anisotropic shrinkage occurred in all compacts with aligned, elongated particles, however, the direction of higher shrinkage was in some cases along the direction of elongation and in other cases in the perpendicular direction depending on the details of the powder compact. A variety of shrinkage behavior, in both preferential shrinkage direction and magnitude, was found depending on microstructural details such as grain and pore shapes, pores distribution, grain alignment, etc. However, the origin of anisotropic shrinkage in all cases is due to annihilations occurring preferentially along grain boundaries oriented predominately in one direction.

[1] P.M. Raj and W.R. Cannon, "Anisotropic Shrinkage in Tape-Cast Alumina: Role of Processing Parameters and Particle Shape," J. Am. Ceram. Soc., 82 [10] 2619-25 (1999).
[2] H. T. Sawhill, R. H. Jensen, and K. R. Mikeska, "Dimensional Control in Low-Temperature Cofired Ceramic Multilayers"; pp. 611–28 in Ceramic Trans-actions, Vol. 15, Materials and Processes in Microelectronic Systems. Edited by K. M. Nair, R. Pohanka, and R. C. Buchanan. American Ceramic Society, Westerville, OH, 1990.
[3] H. Watanabe, T. Kimura, and T. Yamaguchi, "Particle Orientation during Tape-Casting in the Fabrication of the Grain-Oriented Bismuth Titanate," J. Am.Ceram. Soc., 72 [2] 289–93 (1989).
[4] L. E. Sanchez, "Electrical, Mechanical and Thermal Characterization of a Co-fired Multilayer Substrate Processed from Sol–Gel Silica"; pp. 387–97 in Advances in Ceramics, Vol. 26, Ceramic Substrates and

Packages for Electronic Applications. Edited by M. F. Yan, K. Niwa, H. M. O'Bryan, Jr., and W. S. Young. American Ceramic Society, Westerville, OH, 1989.

[5] P. Nahass, R. L. Pober, W. E. Rhine, W. L. Robbins, and H. K. Bowen, "Prediction and Explanation of Aging Shrinkage in Tape-Cast Ceramic Green Sheets," J. Am. Ceram. Soc., 75 [9] 2373–78 (1992).

[6] P. Nahass, R. L. Pober, W. E. Rhine, W. L. Robbins, and H. K. Bowen, "A Comparison of Aqueous and Nonaqueous Slurries for Tape-Casting and Dimensional Stability in Green Tapes"; pp. 355–64 Ceramic Transactions, Vol. 15, Materials and Processes in Microelectronic Systems. Edited by K. M. Nair, R. Pohanka, and R. C. Buchanan. American Ceramic Society, Westerville, OH, 1990.

[7] M. J. Cima, "Anisotropic Behavior of Tape Cast Ceramic Sheets"; presented at the 100th Annual Meeting of the American Ceramic Society, Cincinnati, OH, May 4, 1998 (International Symposium on Multilayer Electronic Ceramic Devices, Paper No. SXIII-011-98).

[8] G. F. Hait and R. W. Nufer, "Process for the Elimination of Dimensional Changes in Green Ceramic Sheets," U.S. Pat. No. 3 953 562, April 27, 1976.

[9] H. A. Exner and E. A. Geiss, "Anisotropic Shrinkage of Cordierite-Type Glass Powder Cylindrical Compacts," J. Mater. Res., 3 [1] 122–25 (1988).

[10] A. R. Boccaccini, P. A. Trusty, and D. M. R. Taplin, "Anisotropic Shrinkage of Barium–Magnesium Aluminosilicate Glass Powder Compacts during Sintering," Mater. Lett., 24 [7] 199–205 (1995).

[11] S. J. Stedman, J. R. G. Evans, R. J. Brook, and M. J. Hoffmann, "Anisotropic Sintering Shrinkage in Injection-Moulded Composite-Ceramics," J. Eur. Ceram. Soc., 11 [6] 523–32 (1993).

[12] K. Uematsu, H. Ito, S. Ohsaka, H. Takahashi, N. Shinohara, and M. Oku-miya, "Characterization of Particle Packing in an Injection Molded Green Body," J. Am. Ceram. Soc., 78 [11] 3107–109 (1995).

[13] K. Uematsu, S. Ishaka, N. Shinohara, and M. Okumiya, "Grain-Oriented Microstructure of Alumina Ceramics Made through the Injection Molding Process," J. Am. Ceram. Soc., 80 [5] 1313–15 (1997).

[14] J. Huber, W. Krahn, J. Ernst, A. Bocker, and H. J. Bunge, "Texture Formation in Al 2 O 3 Substrates," Mater. Sci. Forum, 157–169, 1411–16 (1994).

[15] T. Zhang, S. Blackburn, and J. Bridgwater, "Debinding and Sintering Defects from Particle Orientation in Ceramic Injection Moulding," J. Mater. Sci., 31 [11] 5891–96 (1996).

[16] R. Greenwood, E. Roncari, and C. Galassi, "Preparation of Concentrated Aqueous Suspensions for Tape Casting," J. Eur. Ceram. Soc., 17 [12] 1393–401 (1997).

[17] P.M. Raj, A. Odulena and W.R. Cannon, "Anisotropic shrinkage during sintering of particle-oriented systems – numerical simulation and experimental studies," Acta Mater., 50 2559-2570 (2002).

[18] W. Zhang and J.H. Schneibel, "The Sintering of Two Particles by Surface and Grain Boundary Diffusion – A Two Dimensional Numerical Study," Acta metal. Mater. 43[12] 4377-4386 (1995).

[19] V. Tikare, M.V. Braginsky and E.A. Olevsky, "Numerical Simulation of Solid-State Sintering: I, Sintering of Three Particles," J. Am. Ceram. Soc., 86[1] 49-53 (2003).

[20] M.P. Anderson, D.J. Srolovitz, G.S. Grest, and P.S. Sahni,, "Computer Simulation of Grain Growth - I. Kinetics," Acta Metall. 32 [5] 783-791 (1984).

[21] E.A. Holm, James A. Glazier, D.J. Srolovitz, G.S. Grest, "Effects of Lattice Anisotropy and Temperature on Domain Growth in the Two-Dimensional Potts Model," Phys. Rev. A, 43 [6] 2662-2668 (1991).

[22] N. Metropolis, A.W. Rosenbluth, M.N. Rosenbluth, A.N. Teller and E. Teller, "Equation of State Calculations by Fast Computing Machines," J. Chem. Phys., 21 1087-1092 (1953).

[23] V. Tikare and E.A. Holm, "Simulation of Grain Growth and Pore Migration in a Thermal Gradient," J. Am. Ceram. Soc., 81[3] 480-484 (1998).

[24] R.T. DeHoff, "Stereological Theory of Sintering," Science of Sintering ed. by D.P. Uskokovic et al, 55-71, Plenum Press, New York (1989)

[25] D.L. Johnson, "New Method of Obtaining Volume, Grain-Boundary, and Surface Diffusion Coefficients from Sintering Data," J. Appl. Phys., 40 [1] 192-200 (1969).

[26] B.H. Alexander and R.W. Balluffi, "The Mechanism of Sintering of Copper", Acta Metall. 5, 666-677 (1957).

[27] Y. Limoge and J.L. Bocquet, "Monte Carlo Simulation in Diffusion Studies: Time Scale Problem," Acta Metall. 36 [7] 1717-1722 (1988).

Distribution:

5		Eugene Olevsky Department of Mechanical Engineering College of Engineering San Diego State University 5500 Campanile Drive San Diego, CA 92182-1323
5		D. Lynne Johnson Department of Materials Science & Engineering Northwest University 2225 N. Campus Dr. Evanston, IL 60208-3108
1	MS 0511	Duane Dimos, 01020
5	MS 0847	J. Guadalupe Arguello, 09126
1	MS 0847	Rod May, 09126
1	MS 0885	Grant Hefflefinger, 01802
1	MS 0889	Jill Glass 01843
1	MS 0889	Sandy Monroe, 01843
1	MS 0889	Raj Tandon, 01843
1	MS 0889	Chad Watson 1843
1	MS 0959	Chris DiAntonio 14192
1	MS 0959	Roger Moore, 14192
1	MS 0959	Bob Poole, 14171
1	MS 0959	Tom Swiler, 14171
1	MS 0959	Fernando Uribe, 14171
1	MS 0959	Pin Yang, 14192
1	MS 0961	Carol Adkins, 14101
1	MS 1411	Nelson Bell, 01846

5	MS 1411	Michael Braginsky, 1834
5	MS 1411	Terry Garino, 01843
1	MS 1411	H. Eliot Fang, 1834
1	MS 1411	Jun Liu, 1846
1	MS 1411	Bruce Tuttle 01843
1	MS 1411	Jim Voigt 01846
10	MS 1411	Veena Tikare, 1834
1	MS 1349	Denise Bencoe, 1843
1	MS 1349	Kevin Ewsuk 01843
1	MS 1349	Bill Hammetter, 1843
1	MS 1349	Ron Loehman, 01843
2	MS 9018	Central Technical Files, 8945-1
1	MS 0899	Technical Library, 9616
1	MS 0323	D Chavez, LDRD Office, 1011